

AD \_\_\_\_\_

Award Number: W81XWH-08-2-0140

TITLE: Mission Connect Mild TBI Translational Research Consortium

PRINCIPAL INVESTIGATOR: Ponnada A. Narayana, PhD

CONTRACTING ORGANIZATION: University of Texas Health Science Center at Houston  
Houston, TX 77030-3900

REPORT DATE: August 2013

TYPE OF REPORT: Final

PREPARED FOR: U.S. Army Medical Research and Materiel Command  
Fort Detrick, Maryland 21702-5012

DISTRIBUTION STATEMENT: Approved for Public Release;  
Distribution Unlimited

The views, opinions and/or findings contained in this report are those of the author(s) and should not be construed as an official Department of the Army position, policy or decision unless so designated by other documentation.

REPORT DOCUMENTATION PAGE				Form Approved OMB No. 0704-0188	
Public reporting burden for this collection of information is estimated to average 1 hour per response, including the time for reviewing instructions, searching existing data sources, gathering and maintaining the data needed, and completing and reviewing this collection of information. Send comments regarding this burden estimate or any other aspect of this collection of information, including suggestions for reducing this burden to Department of Defense, Washington Headquarters Services, Directorate for Information Operations and Reports (0704-0188), 1215 Jefferson Davis Highway, Suite 1204, Arlington, VA 22202-4302. Respondents should be aware that notwithstanding any other provision of law, no person shall be subject to any penalty for failing to comply with a collection of information if it does not display a currently valid OMB control number. <b>PLEASE DO NOT RETURN YOUR FORM TO THE ABOVE ADDRESS.</b>					
1. REPORT DATE August 2013		2. REPORT TYPE Final		3. DATES COVERED 1 August 2008 – 31 July 2013	
4. TITLE AND SUBTITLE Mission Connect Mild TBI Translational Research Consortium				5a. CONTRACT NUMBER W84XWH-08-2-0140	
				5b. GRANT NUMBER W84XWH-08-2-0140	
				5c. PROGRAM ELEMENT NUMBER	
6. AUTHOR(S) Ponnada A. Narayana, PhD  E-Mail:				5d. PROJECT NUMBER	
				5e. TASK NUMBER	
				5f. WORK UNIT NUMBER	
7. PERFORMING ORGANIZATION NAME(S) AND ADDRESS(ES) University of Texas Health Science Center at Houston 7000 Fannin St., Ste 902 Houston, TX 77030-3900				8. PERFORMING ORGANIZATION REPORT NUMBER	
9. SPONSORING / MONITORING AGENCY NAME(S) AND ADDRESS(ES) U.S. Army Medical Research and Materiel Command Fort Detrick, Maryland 21702-5012				10. SPONSOR/MONITOR'S ACRONYM(S)	
				11. SPONSOR/MONITOR'S REPORT NUMBER(S)	
12. DISTRIBUTION / AVAILABILITY STATEMENT Approved for Public Release; Distribution Unlimited					
13. SUPPLEMENTARY NOTES					
14. ABSTRACT  Both human and animal MRI scans were performed as a part of specific aims 1 and 2. Two types of animal studies were performed. In the first study we investigated the effect of hemorrhagic shock on animals with traumatic injury. In the second study we investigated the neuroprotective effects of Epo on the injury outcome. In humans MRI data were acquired on both orthopedic controls and mTBI subjects at baseline (within 24 hours after injury) and at three months. The multi-modal MRI measures included include regional and global volumetry using tensor-based morphometry, tissue microstructural integrity using diffusion tensor imaging (DTI), and T2-weighted images for lesion volumes in animals, and magnetic resonance spectroscopy (MRS) for investigating the metabolic changes, and magnetization transfer imaging (MTR) for assessing the state of myelin (only in humans). In animals with hemorrhagic shock, significant atrophy was detected in some gray matter structures, including the ipsilateral parietal cortex and parts of amygdaloid nucleus and suprachiasmatic nucleus away from the injury site. Significant reduction in FA in the white matter tracts closest to site of injury: ipsilateral external capsule, internal capsule, splenium, body and genu of corpus callosum were also observed. Based on MRS, Epo appears to show some neuroprotective effect. In humans, mean diffusivity (MD), based on DTI, showed group differences between orthopedic controls and mTBI subjects at baseline. These differences appear to resolve on the month 3 scans. We did not observe any group differences on any of the other MRI measures. These studies resulted in two abstract and one publication. Two more manuscripts are under preparation.					
15. SUBJECT TERMS mTBI, MRI, MRS, DTI, MTR, hemorrhagic shock, neuroprotection					
16. SECURITY CLASSIFICATION OF:			17. LIMITATION OF ABSTRACT	18. NUMBER OF PAGES	19a. NAME OF RESPONSIBLE PERSON
a. REPORT	b. ABSTRACT	c. THIS PAGE			USAMRMC
U	U	U	UU		19b. TELEPHONE NUMBER (include area code)

## Table of Contents

	<u>Page</u>
Introduction.....	4
Body.....	4 – 10
Key Research Accomplishments.....	9
Reportable Outcomes.....	9
Conclusion.....	10
References.....	
Appendices.....	8 – 20

## Section 2:

**2.I.A. Introduction:** The overall objective of this core is to assist investigators with their MR imaging/spectroscopy (MRI/S) needs. Specifically, this core will help investigators with the design and implementation of MRI/S protocol, acquisition of the MRI/S data, and analysis.

**Specific Aims:** This is a core facility for this project and the specific aims are described in the individual projects. The specific aims of the projects supported by the core are:

**Specific Aim #1.** *To characterize animal models of mild traumatic brain injury (MTBI) in order to mimic the neurobehavioral deficits observed in human MTBI patients (Investigators: Pramod Dash, Ph.D., John Holcomb, M.D., Douglas DeWitt, Ph.D., Claudia Robertson, M.D).*

**Specific Aim #2:** To improve the diagnosis of MTBI, developing more objective criteria in the early postinjury period as well as in the chronic condition (*Investigators: Harvey Levin, Ph.D., Jill Hunter, Ph.D., Elizabeth Wilde, Ph.D.*)

**Specific Aim #2.1:** To study early (<24 hr) diagnosis of MTBI and differentiation of its sequelae related to brain injury from PTSD symptoms present in MTBI and in orthopedic injury (OI) groups studied over a six month follow-up interval.

**Specific aim #2.2:** To study late (>48hr) diagnosis of MTBI and differentiation of MTBI and PTSD (*Investigators: Andrew Papanicolaou, Ph.D., Joseph Brier, Ph.D., Eduardo Castillo, Ph.D.*).

## 2.II Overall Progress:

### 2.II.A Specific Aim 1: MRI of Traumatic Brain Injured Rats Animal Studies:

All the animal scans were performed using a 7T Bruker MRI scanner with 30 cm horizontal bore. Animals were scanned while under isoflurane anesthesia. For MRI scans the animals were placed on a custom built Plexiglas table that was inserted into the magnet bore. The animals' body temperature was maintained using warm air (temperature maintained using a feedback circuit) and the vital signs were continuously monitored throughout the MRI scan. Images were acquired using a combination of whole body and local radio frequency (RF) coils. The MRI protocol included: 1) scout images for animal positioning, 2) 3D T1-weighted images, 3) dual echo RARE images, 4) DTI, and MRS. Similar to human studies, the MRI data was used to determine regional morphometry, DTI-based measures, and morphometry.

- 1) Lesion volumes were determined for all the groups using the high resolution long echo RARE images
- 2) Diffusion weighted images were analyzed to determine the fractional anisotropy and radial, axial, and mean diffusivities.

- 3) The ratios of N-acetyl aspartate (NAA)/Creatine (Cr) and Choline (Cho)/Cr were determined using the magnetic resonance spectroscopy. NAA is considered to be axonal/neuronal marker, while Cho is marker for membrane integrity.
- 4) Post-contrast images for detecting regional blood-brain-barrier compromise and angiogenesis.

**MRI Morphometry and Diffusion Tensor Imaging in Cortical Impact Model With and Without Hemorrhagic Shock:** As described in the year 2 and 3 annual progress report we completed the morphometric and the diffusion tensor imaging (DTI) in cortical impact injury with and without hemorrhagic shock. Significant atrophy was detected in some gray matter structures, including the ipsilateral parietal cortex and parts of amygdaloid nucleus and suprachiasmatic nucleus away from the injury site. Significant reduction in FA in the white matter tracts closest to site of injury: ipsilateral external capsule, internal capsule, splenium, body and genu of corpus callosum were also observed. The observed regional atrophy in the gray matter areas along with the changes in white matter tract integrity could help gain insight into the pathology underlying post-traumatic disorders. A manuscript based on this work was communicated to Journal of Neurotrauma for publication. However, the reviewers felt that increasing the number of animals would improve the robustness of the results. Therefore, we have scanned additional six animals in each group and begun analyzing the data again. We anticipate completing the analysis in the next few weeks. Once the histology results are available, we will start correlating the MRI with histology.

**Effect of Epo Treatment:** A total of 72 Long Evans rats were included in this study (it was erroneously stated in the last year progress report that 80 animals were scanned), divided into three groups: sham, saline-treated, and Epo-treated. Three animals died during the scan (one each in saline group, Epo at 21 days, Epo at 28 days). Therefore, the actual number of animals on which the MRI data was acquired was 69. The sham group consisted on eight animals, which were scanned 4 weeks after the sham procedure. The groups of saline- and Epo-treated animals were subdivided into four groups. Each of these subdivided groups (n=8) were scanned 1, 2, 3, or 4 weeks after injury; the studies were not longitudinal.

Contrast enhanced T1-weighted MRI did not reveal any compromised blood brain barrier at any time point. The spectroscopically determined ratios of N-Acetyl aspartate/Creatine (NAA/Cr) or Choline/Creatine did not show significant differences between ipsi- and contralateral regions at four weeks post impact. However, at three weeks post impact, there was a transient and significant drop of the NAA/CR ratio in saline treated animals compared to Epo-treated animals at this time point. The contusion volumes of the three groups were not significantly different from each other at four weeks. However, the average contusion volume of the saline treated animals was at four weeks significantly larger than that measured in the same group at two weeks (not shown). Only the DTI metrics showed at four weeks significant differences and these were observed exclusively in the ipsilateral hemisphere: The FA of the

fimbria in saline treated animals was significantly smaller than that of sham operated animals (Fig.1 left). The mean diffusivity (MD) of the cortex was significantly larger in the saline treated animals than in the Epo-treated animals (Fig.1 middle). The radial diffusivities (RD) of the external capsule (ex caps) and cortex were significantly larger in the saline treated animals than in the sham operated animals. Also the RD of the cortex was significantly larger in saline- than in Epo-group.

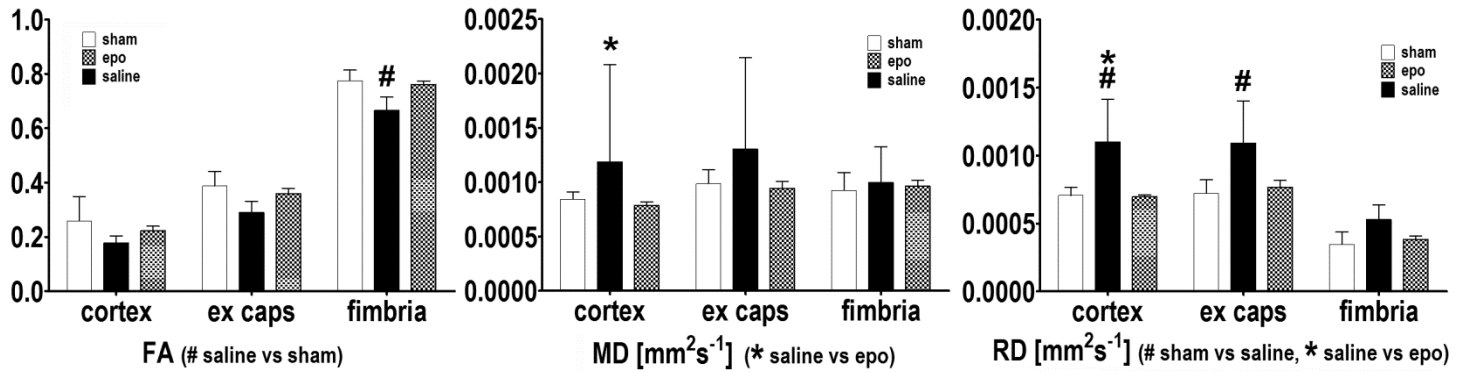


**Figure 1:** Bar plots of FA (left), MD (middle), and RD (right). The analysis was performed with two way ANOVA and a Bonferroni post-test ( $P < 0.05$ ). The analysis included also contralateral structures, internal capsule (ipsi- and contralateral), splenium, and genu. These results are not displayed because their differences were not significant. The ipsilateral structures which had significant differences between the three groups at four weeks were the fimbria (FA), cortex (MD and RD), and external capsule (RD).

We are waiting for the histology results for manuscript preparation.

**Specific Aim 2 MRI of mTBI Subjects:** The human MRI scans are performed on a Philips 3T MRI that is equipped with 80 mT/m gradient system and 32 channel receiver system. The MRI scans were performed using the 8 channel head coil. The MRI protocol includes: 1) scout imaging for locating the brain and prescribing the subsequent MRI scans, 2) 3D T1-weighted MPRAGE, 3) diffusion tensor imaging (DTI), 4) 3D FLAIR, 5) dual gradient recalled echo images (DGRE), 6) susceptibility-weighted images (SWI), and 7) 2D proton magnetic resonance spectroscopy (MRSI). All the image analysis was performed using either locally developed software and/or publicly available software packages. The MRI analysis includes: 1) regional morphometry, 2) DTI-based metrics that include fractional anisotropy (FA), mean (MD), axial (AD), and radial diffusivity (RD), 3) magnetization transfer ratio (MTR), 4) ratios of the metabolites, choline (Cho)/creatine and n-acetyl aspartate (NAA)/Cr.

Regional morphometry was determined using the 3D MPEAGE images based on tensor-based morphometry (TBM) in combination with nonlinear registration that is diffeomorphic and inverse consistent, and in-house developed software. The DTI measures were determined using

the diffusion-weighted images acquired with 32 gradient directions. The data was analyzed using the voxel-based morphometry (VBM), tract based spatial statistics (TBSS), and region-of interest analysis. The MRSI data was analyzed using the LC model package that is a commercial software package along with in-house developed software. The MTR was determined on a voxel-by-voxel basis using in-house developed software. The FLAIR, DGRE, and SWI were qualitatively evaluated for the presence of incidental pathology and hemorrhage.

The number of MRI scans performed so far is summarized in Table 1.

**Table 1: Number of subjects who underwent MRI scans at baseline and 3 months**

Procedure	Visit	# Visits	Attempted?				Attempted, but Unsuccessful				Total # Not Completed*		Total # Completed**	
			Yes	%	No	%	Yes	%	Yes	%	#	%	#	%
MRI	Baseline	164	158	96%	5	3%	1	1%	2	1%	7	4%	157	96%
	3 Month	138	135	98%	4	3%					4	3%	135	98%
<b>Total # Procedures</b>			<b>911</b>	<b>95%</b>	<b>36</b>	<b>4%</b>	<b>5</b>	<b>&lt;1%</b>	<b>15</b>	<b>2%</b>	<b>51</b>	<b>5%</b>	<b>907</b>	<b>95%</b>

\*Attempted=No + Unsuccessful 2 tries

\*\*Attempted=Yes + Unsuccessful 1 try (but eventually completed)

### **Baseline comparison (mTBI vs. orthopedic control):**

At baseline, TBSS analysis showed that the mTBI subjects A+D; A: subjects who were on medication and have MRI; T: subjects who had only MRI scans) had significantly higher MD than the orthopedic control (O) subjects in several neural pathways or WM regions, which include internal capsule (ic), external capsule (ec), superior region of corona radiata (scr), anterior region of corona radiata (acr), posterior region of corona radiata (pcr), inferior fronto-occipital fasciculus (ifo), inferior longitudinal fasciculus (ilf), forceps major and forceps minor of corpus callosum (cc), superior longitudinal fasciculus (slf), and cortical spinal track (cst). With FWE multiple comparison correction ( $p < 0.05$ ), regions that showed significant difference were all on the right side of the brain. The left side brain appeared to have higher MD in similar regions although the difference could only be observed without FWE correction, indicating a weaker effect than the right side. On TBSS we did not find any regions in the brain with significantly lower MD in the mTBI subjects with or without FWE correction.

TBSS analysis also indicated that the mTBI subjects had higher AD and RD than the orthopedic control subjects, in similar regions where higher MD was found. However again, the difference could only be observed without FWE correction ( $p < 0.05$ ). AD showed more significant increase in scr/pcr regions while RD showed more significant increase in plic, ifo and acr regions. In terms of FA, no significant difference was detected between mTBI subjects and orthopedic controls even without FWE correction.

To verify the TBSS results with gold-standard ROI analysis in the native space, three ROI's were placed on each side of the brain in regions where higher MD was found in the mTBI subjects. The ROI's were placed on ec, plic, and scr. They were selected among all the candidate regions because of their higher significance level, larger proportion of total area showing significant changes, easier to identify and more reliable to draw.

Consistent with TBSS results, all three ROI's on the right side of brain showed significant higher MD in the mTBI subjects ( $p < 0.05$ ). Right scr showed significantly higher AD while right ec, plic showed significantly higher RD in the mTBI subjects ( $p < 0.05$ ). None of the ROI's on the left side showed any significant difference between orthopedic controls and mTBI subjects although MD, AD, RD did appear to be higher in the mTBI subjects in almost all cases. For FA, none of the ROI's on either side showed any significant difference between orthopedic controls and mTBI subjects although right ec and plic appeared to be lower in the mTBI subjects.

**Longitudinal Comparison (baseline vs. follow-up):** Longitudinal comparison was performed only on group T and O, since we are blind to treatment in group A. With FWE correction, TBSS analysis failed to detect any significant difference in any DTI measures between baseline mTBI group and follow-up mTBI group on either side of the brain. Without FWE correction, however, it appeared that MD decreased at follow-up in a few WM regions including plic, ec and AD also decreased in some WM regions including cc, ec, acr/scr/pcr, plic. The effect appears to be stronger and more widespread on the right side of the brain.

ROI analysis was also used for comparing baseline T group and follow-up T group. The same set of ROI's was used as before. Interestingly, right plic showed significantly higher FA and significantly lower MD and RD in the follow-up T group than in the baseline T group ( $p < 0.05$ ). Because AD value of the right plic was virtually same at baseline and at follow-up, decrease in RD should be the main cause for the decrease in MD and the increase in FA after 3 months of recovery from mTBI.

For verification purpose, orthopedic controls at the two time points were also compared. TBSS found no significant difference in any DTI measures between baseline controls and follow-up controls on either side of the brain, with or without FWE correction. Similarly, ROI analysis also found no significant difference in any DTI measures between the two time points. This basically suggests the temporal stability of the data.

Based on the analyses on the above groups, we failed to observe and group or temporal differences in MRS, MTR, and morphometric measures.

**Response to EAB feedback:** No concerns were expressed by the External Advisory Board about the MRI core.

**Manuscript Preparation:**



The manuscript “Mild Traumatic Brain Injury with Hemorrhagic Shock: DiffusionTensor Imaging And Tensor Based Morphometry” was communicated for publication. This manuscript was returned with a major concern about the number of animals. We have now increased the number of animals. We will revise the manuscript as soon as the analysis is complete and histology results are available.

The analysis of MRI data on epo treated analysis is complete. As soon as Dr. Robertson’s group completes the histology and neurobehavioral analysis, a manuscript describing these results will be prepared for publication.

The MRI analysis on all the mTBI patients scanned so far is completed. Voxel-wise analysis is used for an unbiased estimation of differences between mTBI and normal subjects. We started working on a manuscript summarizing these results.

### **Key Research Accomplishments:**

- Completed 158 MRI scans at baseline and 135 at 3 months. Developed and implemented sophisticated atlas based image analysis techniques for automatic analysis of morphometry, DTI, and MTR for both humans and rodents.
- Completed morphometric and DTI analysis in traumatically injured animals with and without hemorrhagic shock.
- Completed the scans on 80 animals for investigating the effect of epo treatment using multi-modal MRI
- Completed morphometric, DTI, MTR, and MRS on the subjects recruited so far.

### **Reportable Outcomes:**

Hui C, Esparza-Coss E, Narayana PA Improved 3D Look-Locker Acquisition Scheme and Angle Map Filtering Procedure for T1 Estimation. NMR in Biomed (Accepted for publication)

Two abstracts were presented at the International Society of Magnetic Resonance in Medicine

### **Plans for Next Year**

While the role of MRI core ended on 7/31/2013, we will continue with scanning as more subjects are enrolled and complete the analysis concurrently. We will get together with Dr. Levin’s group for correlating various MRI measures with neuropsychological evaluation. We will continue to scan animals as needed by the investigators. One such need could be the characterization of blast injury model by using longitudinal in vivo MRI. The MRI measures that could help in characterizing this model include lesion evolution and blood-brain-barrier integrity. Being a core we have to depend on the other investigators for recruiting patients and providing animals.

We will begin working on at least three manuscripts.

**Problems:**

None

**Conclusions:**

Studies on structural and regional morphometric changes in brain after cortical impact injury exacerbated by secondary brain insult of hemorrhagic shock were expanded by including more number of animals. We have also completed the MRI scans and analysis for investigating the effect of epo on lesion volume and neuroprotection.

So far we have scanned 76 mTBI subjects with and without treatment and 47 orthopedic controls at baseline. We completed the image analysis on all the subjects scanned so far. The analysis of the results shows a trend in increased regional volumes and FA in certain white matter structures in the acute phase that decreased at 3 months. We did not observe any changes on the other MRI measures (MRS, MTR, and morphometry)

## Serial Atlas-based DTI Study of Mild Traumatic Brain Injury in Adults

Khader M Hasan<sup>1</sup>, Terrell D Staewen<sup>1</sup>, Elisabeth A Wilde<sup>2</sup>, Emmy R Miller<sup>3</sup>, Melissa Frisby<sup>2</sup>, James J McCarthy<sup>4</sup>, Jill V Hunter<sup>5</sup>, Harvey S Levin<sup>2</sup>, Claudia S Peterson<sup>3</sup>, and Ponnada A Narayana<sup>1</sup>

<sup>1</sup>*Diagnostic and Interventional Imaging, University of Texas Health Science Center at Houston, Houston, Texas, United States,* <sup>2</sup>*Physical Medicine and Rehabilitation, Baylor College of Medicine, Houston, Texas, United States,* <sup>3</sup>*Neurosurgery, Baylor College of Medicine, Houston, Texas, United States,* <sup>4</sup>*Emergency Medicine, University of Texas Health Science Center at Houston, Houston, Texas, United States,* <sup>5</sup>*Pediatric Radiology, Texas Children's Hospital, Houston, Texas, United States*

**Introduction:** Mild traumatic brain injury (mTBI) is a major public health concern in both civilian and military populations (1,2). Identifying early neuroimaging markers that relate to cognitive and behavioral changes associated with mTBI is an important application of quantitative MRI modalities (2, 3) such as diffusion tensor imaging (DTI). DTI offers sensitive markers of tissue microstructural integrity that could be used to model the biological sequela of mTBI and in the diagnosis and prognosis of injured subjects (4). However, mTBI causes and effects are heterogeneous and depend on several factors such as age at injury, post-injury interval, injury severity, and location (1,2). In this report, we applied DTI methods serially on cohorts of healthy orthopedic controls and mTBI to characterize regional and global macrostructural and microstructural attributes of white matter (WM), gray matter (GM) and cerebrospinal fluid (CSF) to identify and differentiate patterns of acute and short-term recovery trends. Given that a previous DTI report on mTBI in adults using regions-of-interest (3) implicated the left anterior corona radiata (CR), we analyzed this entire zone using atlas-based methods (5). Our analysis of the cross-sectional and serial data demonstrates dissociation between volumetric (macrostructural) and tissue integrity (microstructural) attributes and show the potential utility of DTI to capture a pattern of transient vasogenic edema using the DTI measurements of the corona radiata.

**Subjects and Methods:** We included 36 mTBI patients (13 females; ages 19-50 years) imaged within 24 hours of injury (Glasgow Coma Scale score 13-15). Nineteen of these patients were imaged at baseline and 3 months. In addition, 37 orthopedic controls (10 females;  $29 \pm 9$  years; age range = 20-49 years) recruited from emergency clinics without head injuries were imaged at baseline and 3 months ( $93 \pm 14$  days). The two cohorts were comparable on gender and age characteristics ( $p=0.85$ ). All MRI studies were performed on a 3T Philips Intera scanner. The diffusion-weighted imaging (DWI) data were acquired using a single-shot spin-echo diffusion sensitized EPI sequence with 32 non-collinear encoding directions,  $b=1000 \text{ sec mm}^2$ ,  $T_R/T_E = 8000/55 \text{ msec}$ . The slice thickness was 3.0 mm with 44 contiguous axial slices covering the entire brain;  $FOV=256 \times 256 \text{ mm}^2$ . **DTI pre-processing:** DWI data were corrected for geometric distortions due to eddy currents using the b0 map which was used for masking or brain extraction BET-FSL (<http://fsl.fmrib.ox.ac.uk/fsl/fslwiki/>), the data were subsequently decoded and diagonalized (4). **Brain Tissue and CSF segmentation and Quantification:** Whole brain CSF (wbCSF) was segmented into ventricular (vCSF) and non-ventricular or sulcal CSF (sCSF), whole brain GM and WM were segmented using a DTI-ICBM atlas-based approach (5, 6). The tissue segmentation utilized contrast between CSF and brain parenchyma on the mean diffusivity (MD) and fractional anisotropy (FA) maps (7). The approach provided volume, and corresponding DTI metrics such as FA, mean, radial and axial diffusivities. Structures were parcellated further into deep/corpus callosum and cortical/lobar which was parcellated into frontal, temporal, parietal, limbic and insular tissue according to the DTI-WM atlas (5). As a representative of deep non-callosal tissue, we focused on the anterior CR (ACR), posterior (PCR) and superior (SCR) segments of the corona radiata bilaterally (3). Regional and global volumes were normalized to the intracranial volume (ICV) obtained from each subject (7, 8). **Statistical Analyses:** Comparisons of regional and global mean values between groups were conducted using analysis-of-variance and generalized linear regression models were used to analyze the scatter of data as age advances.

**Results:** Volume-to-ICV percentage were not different in regional and global CSF, GM and WM. Sulcal and ventricular CSF volumes increased with age in both healthy controls and mTBI (Fig. 1A). As expected, neocortical gray matter decreased with age at comparable rates in both groups. The radial diffusivity of the anterior corona radiata was found to be significantly elevated in mTBI which was not different at 3 months hinting to the possible resolution of edema.

**Discussion:** In this work we analyzed data collected from two age-matched cohorts imaged at two different time points to identify patterns of acute (1 Day) and short term (90 Day) DTI characteristics. Global and regional changes in WM, GM and CSF volumetry were not different between controls and mTBI. Consistent with a previous report (3), subtle changes in WM microstructure due to diffuse axonal injury was detected using the corona radiata diffusivity, hinting that this region is extremely vulnerable due possibly to its low cerebral perfusion. The non-significant serial changes in orthopedic controls indicate stable and reproducible acquisition that assures reliability. The measured regional and global age trends of CSF, WM and GM in both controls and mTBI are consistent with published and predicted trends (8) and assure that the methods used are sensitive to capture changes due to both age and mTBI. The serial or short term trends seen in the mTBI cohort (N=19; baseline vs. 3 months) indicate a pattern of recovery or decrease in both axial and radial diffusivity without a change in FA which could be indicative of possible resolution of transient vasogenic edema as a result of mTBI. The study of long term effects of mTBI on brain structure-function is warranted.

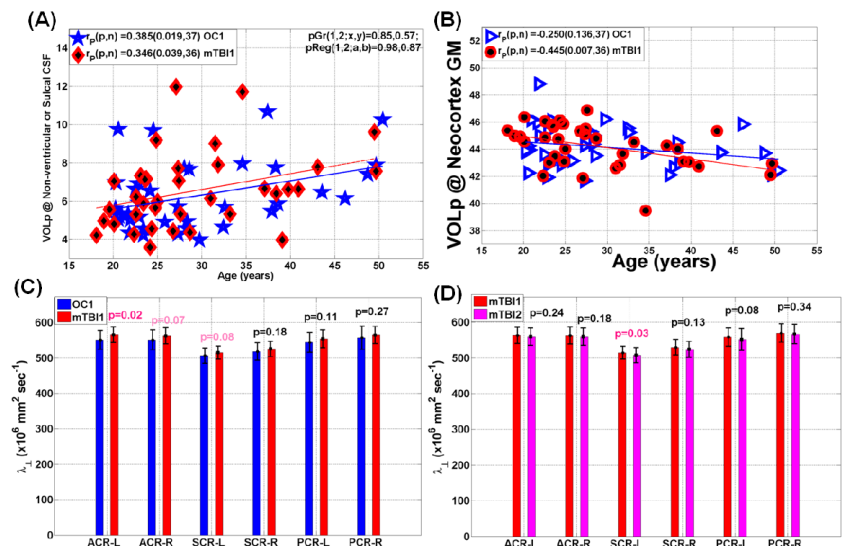


**Figure 1.** Representative scatter plots of global volumetry of (A) sulcal CSF, (B) neocortical GM and bar graphs of regional coronal radiata DTI metrics (C, D) in orthopedic controls (N=36) and mTBI (N=37) both at baseline (Day 1; A, B, C) and serially (D; N=19).

## References

- (1) Bigler ED and Maxwell WL. Brain Imaging Behav. 2012;6(2):108-36.
- (2) Mac Donald CL, et al. N Engl J Med. 2011;364(22):2091-100.
- (3) Niogi SN, et al. Brain. 2008;131(Pt 12):3209-21.
- (4) Levin HS, et al. J Neurotrauma. 2010;27(4):683-94.
- (5) Hasan KM, et al. Comput Biol Med. 2011;41(12):1062-72.
- (6) Mori S, et al. Neuroimage. 2008;40(2):570-82.
- (7) Hasan KM and Frye RE. Hum Brain Mapp. 2011;32(1):107-17.
- (8) Blatter DD, et al. Am J Neuroradiol. 1997;16(2):241-51 & AJNR 1997;18(1):1-10.

# Erythropoietin (EPO) as Treatment of Mild Traumatic Brain Injury: A Multi Modal MRI Study

Kurt Hermann Bockhorst<sup>1</sup>, Robert Garcia<sup>2</sup>, Samson Kujit Gaddam<sup>2</sup>, Claudia S. Robertson<sup>2</sup>, and Ponnada A. Narayana<sup>1</sup>  
<sup>1</sup>DII, University of Texas, Houston, TX, United States, <sup>2</sup>Neurosurgery, Baylor College of Medicine, Houston, TX, United States

## Erythropoietin (EPO) as Treatment of Mild Traumatic Brain Injury: A Multi Modal MRI Study

**Introduction:** It is estimated that 1.7 million people suffer from mild traumatic brain injury (mTBI). MTBI results in physical, cognitive, emotional, and sleep-related disorders. As of now there is no treatment for mTBI. Recent studies in experimental mTBI suggest that Erythropoietin (Epo) may improve the outcome in mTBI. The neuroprotective effect of Epo is mediated by anti-inflammatory, anti-apoptotic, and vascular mechanisms [1-3].

**Material and Methods:** A total of 72 Long Evans rats were included in this study, divided into three groups: sham, saline-treated, and Epo-treated. The sham group consisted on eight animals, which were scanned 4 weeks after the sham procedure. The groups of saline- and Epo-treated animals were subdivided into four groups. Each of these subdivided groups (n=8) were scanned 1, 2, 3, or 4 weeks after injury; the studies were not longitudinal. The animals were anesthetized during the scans with 1.5 to 2.5% Isoflurane in a 70:30 mixture of air and oxygen supplied through a mask. The heads were fixed with mouth and ear bars. The breathing rate, pulse rate, rectal temperature and blood oxygen level were constantly monitored. The body temperature was maintained at 36±0.5°C with a feedback controlled warm air system. The animals were sacrificed after the scans and processed histologically. The result of the histology was not available at the time this abstract was written. The injury model of mTBI was a controlled cortical impact (35psi, impact velocity 3mm/s) through a 10mm-diameter craniectomy. Further details can be found elsewhere [4, 5].

Multi modal MRI that included, anatomical, DTI, MRS, pre- and post-contrast MRI was performed on a 7T Bruker Biospec (USR 70/30 Paravision 5.1 software). 3D Modified Driven-Equilibrium Fourier Transformation (MDEFT) images were acquired for visualizing the anatomy. The TR/TE/TI was 4000ms/5ms/1300ms and the pulse angle was 15°. The spatial resolution was 0.137mm x 0.137mm x 0.5mm. 50 slices were acquired within 27min. Dual echo 2D RARE (Rapid Acquisition and Relaxation Enhancement) images were acquired to measure the contusion volume (TR/TE1/TE2 = 5000ms/23ms/70ms, RARE factor 4, 2 averages, 20 slices, spatial resolution 0.137mm x 137mm x 1mm, scan time 11min). 2D DTI was acquired to study the micro structure of the brain (TR/TE= 10,000ms/27ms, b value 800s/m<sup>2</sup>, 9 b<sub>0</sub>, 42 gradient directions with bipolar icosahedral encoding scheme, 2 acquisitions per direction, resolution 0.27mm x 0.27mm x 0.5mm, 40 slices, and a scan time of 1hr). We used navigator echoes, double sampling, and saturation bands to enhance the DTI data quality. A Point Resolved Spectroscopy Sequence (PRESS) was used to acquire three volumes per animal (2.5mm<sup>3</sup>, location injury site, ipsilateral hippocampus, contralateral hippocampus) with a TR/TE=2500ms/ 20ms, 256 acquisitions, and a scan time of 11min. Finally, T1 weighted Spin Echo images were acquired before and 5 minutes after application of 0.1mmol Gadodiamide (Omniscan) per kg/bw via the tail vein. The TR/TE were 500ms/10ms and the scan time was 2min. The resolution was 0.137mm x 0.135mm x 1mm.

**Results:** Contrast enhanced T1-weighted MRI did not reveal any compromised blood brain barrier at any time point. The spectroscopically determined ratios of N-Acetyl aspartate/Creatine (NAA/Cr) or Choline/Creatine did not have any significant differences between ipsi- and contralateral regions at four weeks post impact. However, at three weeks post impact, there was a transient and significant drop of the NAA/CR ratio in saline treated animals compared to Epo-treated animals at this time point. The contusion volumes of the three groups were not significantly different from each other at four weeks. However, the average contusion volume of the saline treated animals was at four weeks significantly larger than that measured in the same group at two weeks (not shown). Only the DTI metrics showed at four weeks significant differences and these were observed exclusively in the ipsilateral hemisphere: The FA of the fimbria of saline treated animals was significantly smaller than that of sham operated animals (Fig.1 left). The mean diffusivity (MD) of the cortex was significantly larger in the saline treated animals than in the Epo-treated animals (Fig.1 middle). The radial diffusivities (RD) of the external capsule (ex caps) and cortex were significantly larger in the saline treated animals than in the sham operated animals. Also the RD of the cortex was significantly larger in saline- than in Epo-treated animals.

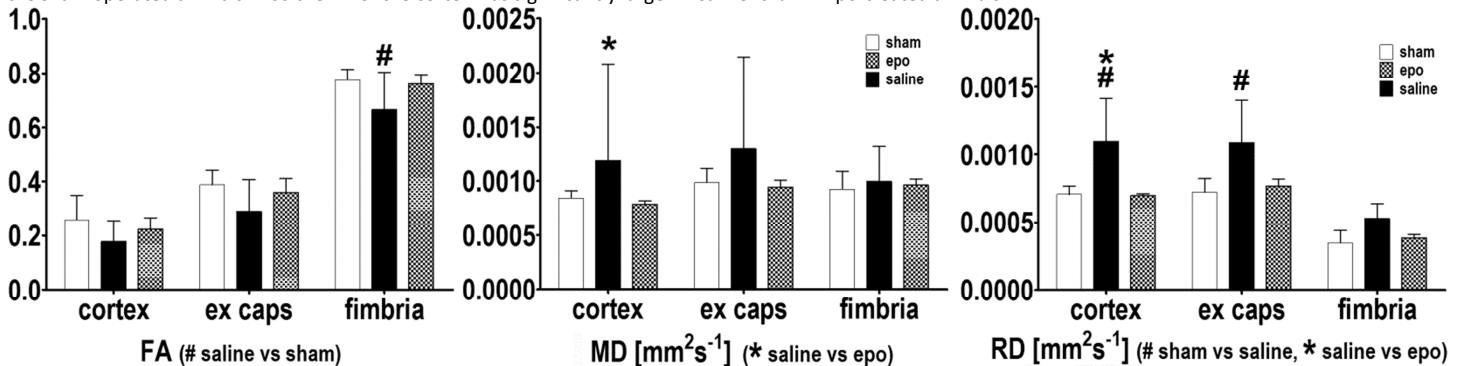


**Figure 1:** Displayed are bar graphs of significant differences in FA (left), MD (middle), and RD (right). The analysis was performed with two way ANOVA and a Bonferroni post-test ( $P < 0.05$ ). The analysis included also contralateral structures, internal capsule (ipsi- and contralateral), splenium, and genu. These results are not displayed because their differences were not significant. The ipsilateral structures which had significant differences between the three groups at four weeks were the fimbria (FA), cortex (MD and RD), and external capsule (RD).

**Conclusion and Discussion:** At four weeks, only the DTI metrics of the ipsilateral hemisphere showed significant differences. Significant differences were found in the cortex, external capsule and fimbria. These structures are closest to the injury site. Decreased FA values indicate in general damage of tissue. Elevated MD and RD indicate enlarged intercellular space, caused possibly by edema and/or loss of tissue. Epo has been described as neuroprotective and that it suppresses intracellular inflammatory processes and apoptosis. It promotes neurogenesis and angiogenesis [1-3]. Due to these characteristics, Epo-treatment appears effective in maintaining the integrity of neural tissue. The absence of BBB leakage confirms the mild character of the injury. DTI proves to be a valuable tool for the analysis of mTBI.

**References:** [1] Lu et al (2005), J Neurotrauma 22, 1011. [2] Siren et al (2001), Proc Natl Acad Sci USA 98, 4044. [3] Villa et al (2003), J Exp Med 198, 971. [4] Robertson et al (2012), J Neurotrauma 29, 1–10. [5] Robertson et al (2012), J Neurotrauma 29, 1156–1166.

# Improved three-dimensional Look–Locker acquisition scheme and angle map filtering procedure for $T_1$ estimation

CheukKai Hui, Emilio Esparza-Coss and Ponnada A. Narayana\*

The three-dimensional (3D) Look–Locker (LL) acquisition is a widely used fast and efficient  $T_1$  mapping method. However, the multi-shot approach of 3D LL acquisition can introduce reconstruction artifacts that result in intensity distortions. Traditional 3D LL acquisition generally utilizes a centric encoding scheme that is limited to a single phase-encoding direction in  $k$  space. To optimize  $k$ -space segmentation, an elliptical scheme with two phase-encoding directions is implemented for the LL acquisition. This elliptical segmentation can reduce the intensity errors in the reconstructed images and improve the final  $T_1$  estimation. One of the major sources of error in LL-based  $T_1$  estimation is a lack of accurate knowledge of the actual flip angle. A multi-parameter curve-fitting procedure can account for some of the variability in the flip angle. However, curve fitting can also introduce errors in the estimated flip angle that can result in incorrect  $T_1$  values. A filtering procedure based on goodness of fit (GOF) is proposed to reduce the effect of false flip angle estimates. Filtering based on GOF weighting can remove probable incorrect angles that result in bad curve fitting. Simulation, phantom and *in vivo* studies have demonstrated that these techniques can improve the accuracy of 3D LL  $T_1$  estimation. Copyright © 2013 John Wiley & Sons, Ltd.

**Keywords:** Look–Locker  $T_1$  mapping; elliptical segmentation; goodness-of-fit weighted filtering

## INTRODUCTION

The spin–lattice relaxation time ( $T_1$ ) is one of the most basic parameters in MRI. Knowledge of the  $T_1$  value is also important in various quantitative MRI techniques, including arterial spin labeling for perfusion measurements and dynamic contrast-enhanced-MRI for vascular permeability assessment.

Traditionally,  $T_1$  maps are generated using the inversion recovery spin echo (IRSE) sequence, which is considered to be the gold standard. However, IRSE-based  $T_1$  measurements involve long scan times and are generally impractical for *in vivo* studies. Different methods have been proposed to accelerate  $T_1$  map acquisition. In general, rapid  $T_1$  measurements fall into two categories: excitation using variable flip angles (VFAs) (1) and fast sampling of the inversion recovery curve (2).

In the VFA method,  $T_1$  is estimated from a set of at least two spoiled gradient recalled echo (SPGR) data acquired with different flip angles. With short TR, the VFA method involves relatively short acquisition times. However, the uncertainty in the flip angle caused by the radiofrequency (RF) magnetic field ( $B_1$ ) inhomogeneity results in significant errors to the  $T_1$  estimation (3,4). As a result, separate  $B_1$  mapping is required to evaluate the  $T_1$  values correctly. In addition, the accuracy of  $T_1$  measurement depends on the choice of flip angles (5,6), and the measurement can suffer from instability if the transverse magnetization is not sufficiently spoiled (7).

Fast sampling of inversion recovery can also be achieved with the Look–Locker (LL) acquisition scheme (8). The LL method monitors the magnetization recovery through  $T_1$  relaxation by continuously acquiring series of images after spin inversion or saturation. The continuous data acquisition can decrease the scan time compared with the traditional inversion recovery

sequence. LL  $T_1$  mapping was originally designed for multi-slice two-dimensional (2D) acquisition (9–12). Generally, 2D sequences have a time advantage over 3D sequences, but they suffer from low signal-to-noise ratio (SNR) and cross-talk. To reduce the 3D LL acquisition time, Henderson *et al.* (13) presented a 3D LL acquisition scheme using a multi-shot approach in which multiple  $k$  lines are sampled in each shot. Since then, many variants of the 3D LL method have been proposed to improve the efficiency of  $T_1$  measurements (14–16). However, as the  $k$  lines for an image are acquired at different time points using the multi-shot approach, intensity artifacts can occur as a result of evolving magnetization (17). Normally, the reconstruction artifacts are reduced by using a centric  $k$ -space encoding scheme. Conventionally, the 3D LL encoding scheme is linear and centric along a single phase-encoding direction (13,15). However, the linear centric encoding scheme is not optimal and can also introduce intensity artifacts that compromise the accuracy of the reconstructed images (18).

\* Correspondence to: P. A. Narayana, Department of Diagnostic and Interventional Imaging, University of Texas Medical School at Houston, 6431 Fannin St., Houston, TX 77030, USA.

E-mail: ponnada.a.narayana@uth.tmc.edu

C. Hui, E. Esparza-Coss, P. A. Narayana  
Department of Diagnostic and Interventional Imaging, University of Texas Medical School at Houston, Houston, TX, USA

**Abbreviations used:**  $B_1$ , RF field; CC, corpus callosum; FOV, field of view; GM, gray matter; GOF, goodness of fit; IRSE, inversion recovery spin echo; LL, Look–Locker; RF, radiofrequency; RMS, root mean square; ROI, region of interest; SNR, signal-to-noise ratio; SPGR, spoiled gradient recalled echo; VFA, variable flip angle; WM, white matter; 2D, 3D, two/three-dimensional.

As a result of  $B_1$  inhomogeneity (13,19), the actual RF angles vary spatially across the image. The accuracy of  $T_1$  computation from the LL acquisition, however, depends on the knowledge of the actual RF flip angles in each voxel. Some published studies (11,19) have proposed the application of a multi-step curve-fitting procedure in which the flip angle map is initially estimated from multi-parameter curve fitting. The estimated flip angle is then smoothed and used as the actual flip angle map in the final curve fit to calculate  $T_1$ . The flip angle estimated from the curve fitting, however, may be inaccurate because the additional parameter in curve fitting increases fitting uncertainty. Unfortunately, simple smoothing methods cannot remove the incorrect flip angles that can still affect the accuracy of the  $T_1$  values.

In this study, we propose elliptical  $k$ -space segmentation for the 3D LL sequence which is centrally encoded along both phase-encoding directions. We also propose a filtering procedure for the flip angle map to improve the accuracy of  $T_1$  measurements. This filter is based on the goodness of fit (GOF) and can remove incorrect angle estimates. These methods are applied to both digital and real phantoms, as well as *in vivo* animal brain, and demonstrate improved results over the traditional 3D LL methods.

## EXPERIMENTAL DETAILS

### 3D LL elliptical segmentation

In the fast 3D LL sequence, an inversion pulse is first applied to invert the longitudinal magnetization, followed by a train of small flip angle pulses to sample the magnetization recovery. Because multiple  $k$  lines within a group are acquired after each

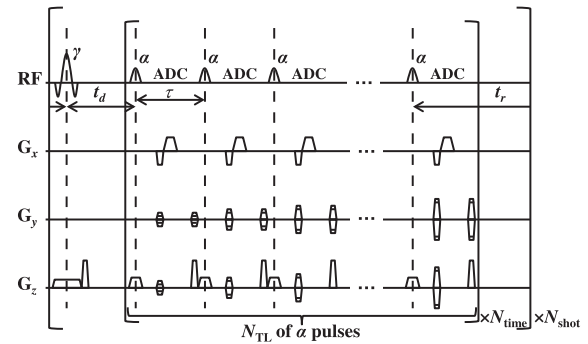


**Figure 1.** Schematic diagram of the proposed elliptical segmented three-dimensional Look-Locker (LL) sequence. After an inversion pulse,  $N_{\text{time}} \times N_{\text{TL}}$   $k$  lines are acquired. Within each shot (external bracket),  $N_{\text{TL}}$  of  $k$  lines are acquired at each time point (internal bracket). In this implementation, both  $G_y$  and  $G_z$  increase with increasing number of  $\alpha$  pulses, whereas a fixed  $G_z$  is employed within each shot in the traditional linear segmented LL acquisition. ADC, analog to digital convertor (data acquisition); RF, radiofrequency.

order of  $k$ -space data acquisition goes from center  $k$  space to outer  $k$  space. The elliptical segmentation scheme ensures that the most centric part of  $k$  space is acquired after the same  $\alpha$  pulse and thus has the same magnetization. As the central  $k$  space contributes more to the signal intensity, the elliptical segmentation can reduce intensity artifacts in the reconstructed images. An illustration of the elliptical centric scheme is shown in Fig. 2.

Assuming perfect spoiling of the transverse magnetization and that the magnetization has reached steady state, the transverse magnetization after the  $n^{\text{th}}$   $\alpha$  pulse can be expressed as follows:

$$M_{\perp}(n) = \sin \alpha M_0 \left\{ \frac{F_E(1 - F_1)}{F_0} + \frac{F_1}{(1 - \cos \gamma \cos \alpha \text{EdEr} F_2)} \left[ 1 - (1 - \cos \gamma) \text{Ed} - \cos \gamma \text{EdEr} + \frac{\cos \gamma \cos \alpha \text{EdEr} F_E(1 - F_2)}{F_0} \right] \right\} \quad [11]$$

inversion pulse, this allows rapid acquisition of 3D images for  $T_1$  estimation. However, as different  $k$  lines are sampled at different magnetization states, the reconstructed image can suffer from intensity artifacts. Here, we assume that  $x$  is the frequency-encoding direction and the two phase-encoding directions are along the  $y$  and  $z$  directions. Traditionally, the  $k_y$  lines for a single  $k_z$  are centrally acquired (13,15). However, such linear  $k$ -space segmentation is not truly centric. It has been shown that the elliptical centric encoding segmentation can produce images superior to those obtained from single-direction centric encoding (18). Therefore, we implemented the elliptical centric encoding acquisition to minimize the reconstruction artifacts.

The 3D LL pulse sequence is depicted in Fig. 1. After the application of an inversion pulse with angle  $\gamma$ ,  $N_{\text{TL}}$   $k$  lines at all the time points  $N_{\text{time}}$  are acquired. An RF pulse of small flip angle  $\alpha$  is applied to sample the recovering magnetization. The repetition time between each  $\gamma$  pulse is  $\text{TR} = t_d + (N_{\text{time}} N_{\text{TL}} - 1)\tau + t_r$ , where  $t_d$  is the initial delay between the  $\gamma$  pulse and the first  $\alpha$  pulse,  $\tau$  is the time between each  $\alpha$  pulse and  $t_r$  is the undisturbed delay after the final  $\alpha$  pulse for magnetization recovery prior to the next  $\gamma$  pulse. The acquisition is elliptically encoded so that the

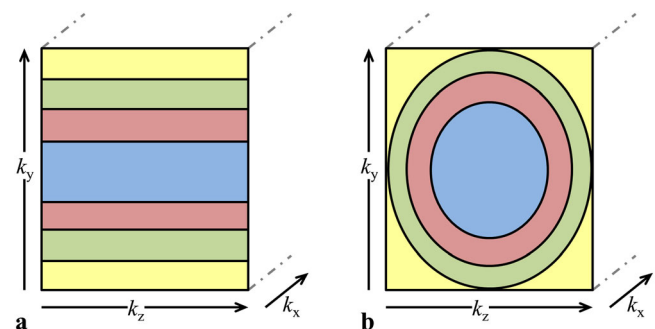


**Figure 2.** Examples of different  $k$ -space segmentation schemes with  $N_{\text{TL}} = 4$  in the three-dimensional Look-Locker (LL) sequence.  $k_y$  and  $k_z$  are the two phase-encoding directions, whereas  $k_x$  is the fully sampled frequency-encoding direction. Regions with different colors in  $k$  space are acquired with different  $\alpha$  pulses. Intensity artifact may occur because different  $k$  space is sampled at different magnetization. (a) The traditional LL scheme is linearly segmented with fixed  $k_z$ . (b) The proposed elliptical segmentation scheme ensures that acquisition is centered in both phase-encoding directions and should provide images with less intensity artifact.



where

$$\begin{aligned} E_{\tau} &= \exp(-\tau/T_1) \\ E_d &= \exp(-t_d/T_1) \\ E_r &= \exp(-t_r/T_1) \\ F_0 &= 1 - \cos \alpha \cdot E_{\tau} \\ F_1 &= (\cos \alpha \cdot E_{\tau})^{n-1} \\ F_2 &= (\cos \alpha \cdot E_{\tau})^{N_{\text{tot}}-1} \\ F_E &= 1 - E_{\tau} \end{aligned}$$

and  $M_0$  is the equilibrium magnetization. The derivation of Equation [1] is presented in the Appendix. As suggested by Henderson *et al.* (13),  $n$  in which the center of  $k$  space is sampled should be assigned as the effective  $n$  of the reconstructed image. Using the elliptical segmentation scheme, the most centric part of  $k$  space is acquired following the first  $\alpha$  pulse, and thus should optimize the correct association between the reconstructed image and its effective  $n$ . Therefore, the final reconstructed images would be associated with  $n = \{1, N_{\text{TL}} + 1, 2N_{\text{TL}} + 1, \dots, (N_{\text{time}} - 1)N_{\text{TL}} + 1\}$ . This optimization would improve the accuracy of the subsequent curve fitting.

### GOF weighted angle filtering

In principle, the  $T_1$  value can be obtained by fitting the LL data in Equation [1] with two parameters ( $M_0$  and  $T_1$ ), provided that the actual RF pulse angles are known. Although the inversion angle of an adiabatic pulse is considered to be sufficiently accurate, the actual flip angle of the RF pulse is not necessarily the same as the nominally prescribed angle, and shows spatial dependence because of the  $B_1$  inhomogeneity. Using incorrect angles in the curve-fitting procedure will lead to inaccurate  $T_1$  values. Curve fitting using three parameters ( $M_0$ ,  $\alpha$  and  $T_1$ ) on a voxel-by-voxel basis can take into account the variation in the actual  $\alpha$ . However, with the additional parameter  $\alpha$ , the curve fitting becomes less robust and could also produce spurious  $\alpha$  and  $T_1$  values. To reduce the effect of incorrect  $\alpha$  estimates, Deichmann (19) spatially smoothed the estimated  $\alpha$  map. The smoothed  $\alpha$  map was considered to be the actual  $\alpha$  map, and was used in the subsequent two-parameter curve fitting. This approach is analogous to the method suggested by Clare *et al.* (20), in which the inversion angle map is smoothed with a Gaussian kernel. Although the smoothing parameters were not mentioned in these publications, these techniques probably employed a spatially weighted averaging to smooth the respective angle maps. However, weighted spatial averaging still cannot remove the incorrect angles from the calculation that can affect the final  $T_1$  estimates.

In this study, we propose a filtering approach weighted by GOF to produce reliable  $\alpha$  estimates. This is a hierarchical multi-step approach in which Equation [1] is first fitted with three parameters ( $M_0$ ,  $\alpha$  and  $T_1$ ) to the coarse resolution image to generate the preliminary  $\alpha$  map. The coarse resolution was used to reduce the processing time and to improve the effective SNR, and hence the consistency of the estimated  $\alpha$  map. As  $\alpha$  is expected to vary smoothly, the use of coarse resolution is justified. The inversion angle  $\gamma$ , which is generated by the adiabatic pulse, is considered to be constant across the image. Assuming that the correct  $\alpha$  estimate can produce better curve fitting to the data,  $\alpha$  which yields a large deviation from the data is likely to be incorrect and should be removed, whereas  $\alpha$  that yields small deviation is likely to be a correct estimate and should be weighted more. The preliminary  $\alpha$  map is therefore

filtered on the basis of GOF of the three-parameter fit. The preliminary coarse  $\alpha$  map is interpolated back to the original resolution and  $\alpha$  in each voxel is filtered with a user-defined spatial kernel using the following equation:

$$\alpha = \left\{ \frac{\sum_i \alpha_i (E_{\text{thre}} - E_i)}{\sum_i (E_{\text{thre}} - E_i)} \mid E_i < E_{\text{thre}} \right\} \quad [2]$$

where

$$E_i = \sqrt{\sum_t (I(i, t) - \hat{I}(i, t))^2} \quad [3]$$

In the above equation, index  $i$  represents all the voxels within the spatial kernel in which  $E_i < E_{\text{thre}}$ , and the time index  $t$  includes all the acquired time points. In the above equation,  $I(i, t)$  represents the signal intensity at time point  $t$  of the coarse voxel in which voxel  $i$  belongs, and  $\hat{I}(i, t)$  is the signal intensity of the fitted curve. Instead of using the more common  $\chi^2$  value as a weighting factor, Equation [3] is used because the  $\chi^2$  weighting includes intensity variance within the coarse voxel. The variance within the coarse voxel is mostly the result of different tissue types in biological samples. It has a relatively small influence on the curve fitting, but can affect the  $\chi^2$  value greatly. Therefore, Equation [3] is preferred to the  $\chi^2$  value. The summation in Equation [2] only includes  $\alpha$  within the kernel that has its corresponding  $E_i$  below a threshold  $E_{\text{thre}}$ , and therefore removes  $\alpha$  values with high fitting error. The weighting factor depends on the difference  $(E_{\text{thre}} - E_i)$ , and so smaller the  $E_i$ , the greater is the corresponding  $\alpha_i$  weighs. The optimal  $E_{\text{thre}}$  is determined in this study using simulations. The filtered  $\alpha$  map is used in the final full-resolution  $T_1$  map calculation employing the two-parameter curve fit.

### Simulations

The software for data processing and simulations was written in IDL 8.1 (ITT Visual Information Solutions, Boulder, CO, USA). All curve-fitting procedures were performed using the MPFIT curve-fitting routine (21).

A 3D Shepp-Logan phantom was used to investigate the quality of image reconstruction employing elliptical LL segmentation, as well as the effectiveness of the GOF filter. The matrix size of the phantom was  $128 \times 128 \times 128$  and was composed of 10 ellipsoidal segments with eight combinations of  $M_0$  and  $T_1$  ( $T_1$  ranged from 750 to 3000 ms). To create the effect of partial volume and to reduce the sharpness of the edges, the phantom was then downsampled to  $64 \times 64 \times 64$  by simple averaging. Figure 3a shows the  $T_1$  map of the  $64 \times 64 \times 64$  Shepp-Logan phantom. The following parameters were used to simulate the LL acquired images:  $\tau = 8$  ms;  $t_d = 10$  ms;  $t_r = 1000$  ms;  $\alpha = 8^\circ$ ;  $\gamma = 180^\circ$ ;  $N_{\text{time}} = 10$ ;  $N_{\text{TL}} = 16$ . These parameters are similar to those used in the phantom studies described below.

To simulate the  $B_1$  inhomogeneity, a synthetic  $B_1$  field was created with the following smoothly varying function:

$$B_1(i, j, k) = \left(1.32 - 0.011(i - 21)^2\right) \times \left(1.14 - 0.016(j - 32)^2\right) \times (0.77 + 0.014(k - 32)^4) \quad [4]$$

where  $i, j, k$  are the pixel indices of the simulated volume. The spatially varying  $\alpha$  was calculated by multiplying Equation [4]

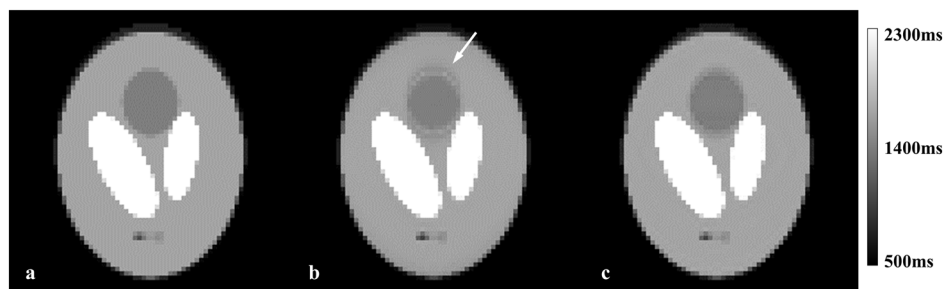


**Figure 3.**  $T_1$  maps of the three-dimensional Shepp-Logan phantom shown in the  $x$ - $y$  plane: (a) original; (b) generated using the Look-Locker (LL) acquisition with linear segmentation; (c) elliptical segmentation. A ripple-like artifact (arrow) is visible in (b), but is considerably reduced in (c).

with the nominal  $8^\circ$  flip angle. This  $B_1$  variation produced a flip angle ranging between  $7.4^\circ$  and  $9.7^\circ$  with an average value of  $8.8^\circ$  within the phantom. The range of  $B_1$  field produced by Equation [4] is in reasonable agreement with a real  $B_1$  field (22). The mean  $\alpha$  was chosen to be different from the nominal  $\alpha$ , so that correct estimation of  $\alpha$  was not a result of its value being close to the nominal value.

Two types of noise were added to the images: intensity-based Gaussian noise and uniformly distributed white noise. The Gaussian noise depends on the inherent image intensity. In this experiment, we applied different levels of Gaussian noise with standard deviations of 2%, 4%, 6%, 8% and 10% of the intensity. The white noise is independent of the intensity and was generated with a mean of zero. The standard deviation of white noise was chosen to be 1% of the mean intensity of the image at the first time point, which has the highest intensity among all time points. All images and noise were created in the image space and the phase information was ignored. The  $k$ -space data were then computed, and segmentation of  $k$ -space was performed using both linear segmentation and the proposed elliptical segmentation. For each noise level, four sets of data were created by generating the random noise four times, to ensure that the results were not affected by the randomness. Images were reconstructed and the magnitude of the signal was used to compute  $T_1$ .  $T_1$  was computed with the multi-step curve-fitting procedure, where the preliminary  $\alpha$  map was first obtained with a three-parameter curve fit. The proposed GOF filter was used to smooth the preliminary  $\alpha$  estimates. For comparison, the preliminary  $\alpha$  map was also smoothed with the Gaussian-weighted spatial averaging method.

### Phantom study

All MRI measurements were performed on a USR70/30 horizontal-bore 7-T MR scanner (Bruker BioSpin, Karlsruhe, Germany). The 3D LL acquisition with elliptical segmentation and linear segmentation were both implemented for this study. In the phantom study, a 71-mm-diameter birdcage resonator was used for both RF transmission and signal reception. Four 12-mm-diameter cylindrical glass vials, filled with water doped with different concentrations of  $\text{NiCl}_2$  (1.2, 0.93, 0.85 and 0.66 mM), served as our phantoms of different  $T_1$  values. As  $T_1$  within each vial was homogeneous, artifacts caused by the  $k$ -space segmentation scheme are expected to be minimal. Therefore, only the elliptical segmentation was used in the phantom study. Different combinations of LL parameters were used to examine the consistency of the LL method. Specifically, the effects of different train length  $N_{\text{TL}}$  and number of time points  $N_{\text{time}}$  were investigated (see Fig. 7 legend). The common acquisition parameters for all the scans were as follows:

TE = 2.2 ms;  $t_d$  = 10 ms;  $t_r$  = 1000 ms;  $\alpha$  =  $8^\circ$ ;  $N_{\text{dummy}}$  = 5; matrix size,  $96 \times 96 \times 48$ ; field of view (FOV),  $35 \times 35 \times 60 \text{ mm}^3$ . The scan time for each of the LL acquisitions was 12.5 min, except for the scan described in Fig. 7b, for which the scan time was 21 min. All the parameters were chosen such that the span over which the inversion recovery being sampled was similar in each scan. A multi-step procedure was employed to compute  $T_1$  with the use of GOF filtering as well as Gaussian-weighted spatial averaging for comparison.  $T_1$  was also computed using IRSE acquisition as the reference standard.  $T_1$  measurements using IRSE were performed only on a single slice to reduce the total acquisition time. The acquisition parameters for the IRSE sequence were as follows: TE/TR = 7.5/10 000 ms; TI = 50, 100, 200, 300, 450, 600, 800, 1000, 1250, 1500, 2000, 2500, 3000 ms; matrix size,  $96 \times 96$ ; in-plane FOV,  $35 \times 35 \text{ mm}^2$ ; slice thickness, 2.5 mm; total scan time, 3.5 h.

### In vivo animal study

*In vivo* LL data were acquired from the acquisition of a normal Sprague-Dawley rat. The protocol of this study was reviewed and approved by the Institutional Animal Welfare Committee. We followed strictly the National Institutes of Health Guide for the Care and Use of Laboratory Animals. During the MRI scan, the animal was anesthetized with 2.5% isoflurane, 30% oxygen and medical grade air. Respiration, rectal temperature and heart rate were monitored throughout the scan. The 71-mm-diameter birdcage resonator was used for RF transmission and an in-house-built surface coil was used for RF reception. 3D LL acquisitions (both linear and elliptical segmentations) were acquired with the following parameters: TE = 3.1 ms;  $\tau$  = 9 ms;  $t_d$  = 11.5 ms;  $t_r$  = 1000 ms;  $\alpha$  =  $8^\circ$ ;  $N_{\text{TL}}$  = 16;  $N_{\text{time}}$  = 10;  $N_{\text{dummy}}$  = 5; matrix size,  $128 \times 128 \times 32$ ; FOV,  $25 \times 25 \times 32 \text{ mm}^3$ ; total scan time, 10.5 min.  $T_1$  maps were calculated using the multi-step procedure with the GOF filter and also with the Gaussian-weighted spatial averaging for comparison. IRSE data were acquired on one slice for verification with the following parameters: TE/TR = 7.6/6000 ms; TI = 20, 200, 400, 600, 800, 1000, 1500, 2500 ms; matrix size,  $128 \times 128$ ; in-plane FOV,  $25 \times 25 \text{ mm}^2$ ; slice thickness, 1 mm; total scan time, 1.7 h.

## RESULTS

### Simulation

The relative root-mean-square (RMS) error was used to quantify the overall error within an image. The relative RMS error of a given parameter  $\theta$  in a particular region of interest (ROI) was calculated using:



$$\Delta\theta_{\text{RMS}} = \sqrt{\frac{1}{N} \sum_x \left( \frac{\theta(x) - \theta_0(x)}{\theta_0(x)} \right)^2} \quad [5]$$

where  $\theta(x)$  and  $\theta_0(x)$  are the estimated and actual values of the parameter in the voxel  $x$ , respectively. The summation included all voxels within the ROI, and  $N$  is the total number of voxels in the summation. The relative mean difference between the estimated and actual values was used to assess the error in the parameter value. The errors in the entire image were calculated for each dataset. In addition, we also computed the errors at the edges between structures with different intensity as the reconstruction artifacts are expected to be more prominent at the edges. The edges were identified if the voxels within a  $2 \times 2 \times 2$  region consisted of different combinations of  $M_0$  and  $T_1$ .

The original  $T_1$  map of the Shepp–Logan phantom is shown in Fig. 3a. For comparison, the corresponding maps generated using the linear and elliptical LL segmentation are shown in Fig. 3b, c, respectively. The relative RMS errors in the image intensity and  $T_1$  values in the reconstructed images, using both linear and elliptical segmented LL acquisitions, are summarized in Table 1. This table shows data on noiseless images to emphasize the intensity artifacts inherent in the 3D LL acquisition. The errors in intensity were different at different acquisition time points. Larger errors were observed between the third and sixth images (associated with the 33rd, 49th, 65th and 81st  $\alpha$  pulses). These images were located around the null points in the inversion recovery curves. Therefore, they had lower SNR and were more susceptible to reconstruction artifacts. As the edges are characterized by high spatial frequencies, the RMS errors are expected to be more prominent at the edges. The results shown in Table 1 confirm this. As seen from this table, an overall increase in the RMS errors was observed using the linear LL scheme relative to the elliptical segmented LL scheme. As listed in Table 1, the use of the elliptical segmentation reduced the RMS error in  $T_1$

by 1.3% in the whole image and 1.9% at the edges. The superior performance of the elliptical segmented LL scheme can also be visually appreciated by comparing Fig. 3b with Fig. 3c. In this example, a ripple pattern artifact was seen in the central ellipse in the  $T_1$  map generated using the linear segmentation LL scheme in Fig. 3b. This artifact was greatly reduced using the elliptical segmentation, as shown in Fig. 3c. Figure 4 shows a typical example of data obtained from a voxel outside of the ripple region in Fig. 3. In this example, the  $T_1$  values generated with the elliptical segmentation are closer to the actual values.

The relative mean differences in the image intensity and  $T_1$  values between the LL acquired images and the original images are summarized in Table 2. As can be seen from this table, the

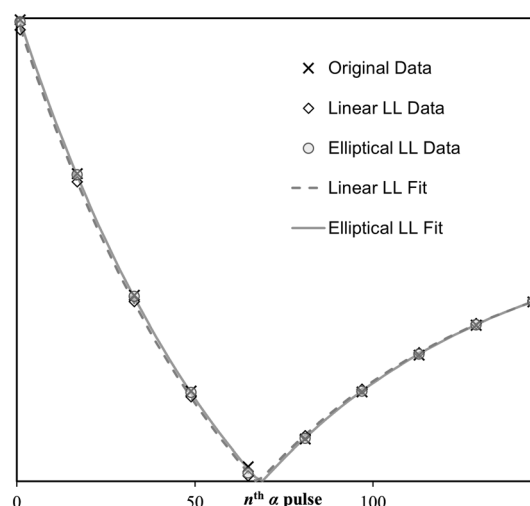


**Figure 4.** The Look–Locker (LL) data of a representative voxel outside of the ripple area in the Shepp–Logan phantom shown in Fig. 3. In this example, there was an underestimation in intensity before and overestimation after the null point in the LL acquisition. The elliptical segmented LL acquisition generally yielded data closer to the original data. In the original image,  $T_1 = 1600$  ms; the linear segmented LL acquisition yielded  $T_1 = 1514$  ms and the elliptical LL acquisition yielded  $T_1 = 1568$  ms. This figure represents data without any noise.

**Table 1.** Relative root-mean-square (RMS) error (%) of the image intensity and  $T_1$  value of the reconstructed images from the Look–Locker acquisition using linear segmentation (linear LL) and the elliptical segmented LL sequence (elliptical LL). Noiseless images were used to emphasize the intensity artifacts as a result of the three-dimensional LL acquisition. Errors of the whole phantom as well as at the edges are presented

Image ( $n^{\text{th}} \alpha$ )	Linear LL		Elliptical LL	
	Whole	Edges	Whole	Edges
1	2.5	3.8	1.9	2.9
17	4.4	6.6	3.9	5.8
33	152.8	228.1	149.1	222.4
49	82.1	122.5	65.6	98.0
65	265.8	394.7	193.1	287.8
81	16.8	23.2	14.7	21.4
97	1.1	1.7	0.7	1.1
113	0.7	1.0	0.4	0.7
129	0.5	0.7	0.3	0.5
145	0.3	0.5	0.2	0.3
$T_1$ error	4.5	6.7	3.2	4.8

**Table 2.** Relative mean difference (%) of the image intensity and  $T_1$  values between the Look–Locker (LL) acquired images and the original images

Image ( $n^{\text{th}} \alpha$ )	Linear LL		Elliptical LL	
	Whole	Edges	Whole	Edges
1	−0.4	−1.1	−0.2	−0.4
17	−1.0	−2.4	−0.7	−1.5
33	13.3	29.6	13.4	29.9
49	14.6	32.6	11.2	24.9
65	35.8	76.4	23.3	50.5
81	−0.5	0.5	0.0	−0.2
97	0.3	0.7	0.1	0.2
113	0.2	0.4	0.0	0.1
129	0.1	0.3	0.0	0.1
145	0.1	0.2	0.0	0.1
$T_1$ error	−1.6	−3.5	−0.9	−2.0

elliptical segmentation also reduced the negative bias by about 0.7% in the whole image and 1.5% at the edges.

Without noise, the voxel-by-voxel three-parameter curve fitting in the presence of  $B_1$  inhomogeneity yielded  $T_1$  errors comparable with those listed in Table 1. However, once noise was introduced, voxel-by-voxel curve fitting using a three-parameter fit resulted in a  $T_1$  error of 13% for elliptical segmented LL images with 6% Gaussian noise. We therefore applied the multi-step procedure to improve the  $T_1$  estimation in the presence of  $B_1$  inhomogeneity. In this study, we chose to downsample the images by a factor of four along each dimension for the initial three-parameter curve fitting (64 times faster processing time). The parameters for the GOF filter and Gaussian-weighted spatial averaging were determined by searching for the parameters that yielded the smallest RMS error in  $T_1$  estimation. The optimal kernel size for the GOF filter was found to be 11 voxels in width. An additional Gaussian-weighted spatial filter with optimal variance  $\sigma^2 = 4.0$  was applied. The optimal threshold  $E_{\text{thre}}$  in Equation [2] was found to be  $2.0 \times \bar{E}$ , where  $\bar{E}$  is the mean  $E_i$  within the kernel. This particular  $E_{\text{thre}}$  removed, on average, about 6% to 18%  $\alpha$  values within the kernel, depending on the noise level. It was also found that the optimal width for the Gaussian-weighted averaging kernel was 17 voxels in order to minimize the  $T_1$  error. In this case, the optimal variance of the Gaussian-weighted spatial filter was found to be  $\sigma^2 = 2.0$ .

All  $\alpha$  map smoothing procedures employed the optimal parameters mentioned above. In general, the  $\alpha$  map obtained from the three-parameter curve fitting, followed by smoothing, showed good consistency at all noise levels tested. Using the Gaussian-weighted spatial averaging, the estimated  $\alpha$  map yielded errors between 1.7% and 2.0%, whereas the  $\alpha$  map smoothed by the GOF filter yielded errors between 0.9% and 1.1%. Application of the GOF filter improved the accuracy of  $T_1$  estimation compared with the Gaussian-weighted spatial averaging. For linear LL acquisition, the GOF filter reduced the  $T_1$  error from 7.2% to 6.8% at 10% Gaussian noise and from 5.5% to 4.7% at 2% Gaussian noise. For elliptical LL acquisition, the GOF filter reduced the errors in  $T_1$  from 6.7% to 6.6% at 10% Gaussian noise and from 4.4% to 4.0% at 2% Gaussian noise. In addition, the GOF filter reduced the negative bias in  $T_1$  estimation by about 2.0% in the linear LL acquisition and about 1.5% in the elliptical LL acquisition.

Figure 5 illustrates the relative RMS errors in  $T_1$  estimation in the presence of  $B_1$  inhomogeneity at different Gaussian noise levels. The proposed LL modifications with elliptical segmentation and GOF filter were compared against the traditional LL method with linear segmentation and Gaussian-weighted spatial averaging.  $T_1$  computation using the proposed modifications showed smaller errors than the traditional methods, and greater improvement was observed at the edges in the Shepp–Logan phantom. The proposed methods also reduced the negative bias of the  $T_1$  values calculated from LL data. On average, the relative mean difference in  $T_1$  using linear segmentation and Gaussian-weighted spatial averaging was about -3.2% for the whole image and -4.9% at the edges for all noise levels. The relative mean difference in  $T_1$  using the proposed LL modifications was about -0.6% for the whole image and -1.7% at the edges.

### Phantom study

The  $T_1$  maps of the Ni-doped water phantoms using the elliptical LL acquisition with the GOF filter are shown in Fig. 6a. The  $T_1$

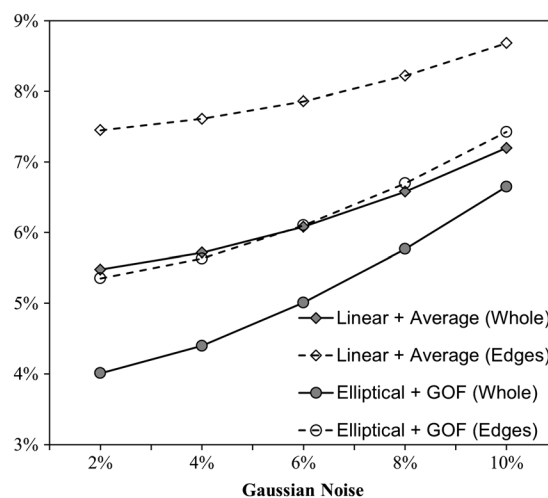


**Figure 5.** The relative root-mean-square (RMS) error of the  $T_1$  values using different Look–Locker (LL) methods in the presence of noise and  $B_1$ -affected flip angle in the Shepp–Logan phantom. Traditionally, the LL method utilizes a linear segmentation scheme and a Gaussian-weighted spatial averaging  $\alpha$  map. We propose to modify the acquisition scheme with elliptical segmentation and the use of a goodness-of-fit (GOF) filter on the  $\alpha$  map. Each data point in the graph represents the average error over the four datasets. The standard deviation at all points is below 0.03% and therefore is not shown in this figure. In general, the RMS error is lower using the proposed techniques (elliptical + GOF), and the improvement is particularly noticeable at the edges.

maps show rather homogeneous  $T_1$  within each of the four tubes. As an example, the LL data, together with the fitted curves obtained from the center voxel in each tube, are shown in Fig. 6b. The values of  $T_1$  obtained from the curve fitting are 817, 962, 1056 and 1259 ms for the four  $\text{NiCl}_2$  concentrations (highest to lowest concentration). Figure 7 shows four representative  $T_1$  distributions in the phantoms using the GOF filtering and Gaussian-weighted spatial averaging methods. These distributions were generated using different acquisition parameters. The parameters were chosen such that much of the inversion recovery was covered in each case. The  $T_1$  values computed from the IRSE acquisition were considered to be the real  $T_1$  values and are shown as vertical lines in Fig. 7. These distributions show that the calculated  $T_1$  value from the LL acquisition was, on average, lower than the real  $T_1$  value. For all the cases except one, the GOF-filtered  $\alpha$  map yielded  $T_1$  estimates closer to the real  $T_1$  value compared with the Gaussian-weighted averaging  $\alpha$  map. The GOF-filtered  $\alpha$  map yielded  $T_1$  values that were within one standard deviation of the real  $T_1$  values 83% of the time, and within two standard deviations 100% of the time. The Gaussian-weighted averaging  $\alpha$  map yielded  $T_1$  values within one standard deviation of the real  $T_1$  values only 21% of the time, but 96% of the time they were within two standard deviations.

The standard deviations of  $T_1$  generated from both smoothing methods were within 3% of their respective mean  $T_1$  values, except in one case in which the standard deviation of one phantom was 5% of its mean  $T_1$  value. In general, using smaller  $N_{\text{TL}}$  and larger  $N_{\text{time}}$  yielded a narrower  $T_1$  distribution or a smaller standard deviation. In most cases, the standard deviations in  $T_1$  values between the two smoothing methods were within 0.1% of each other. However, as shown in Fig. 7a, b, the Gaussian-weighted spatial averaging method occasionally yielded distributions that were noticeably broader. In three cases (third peak in Fig. 7b

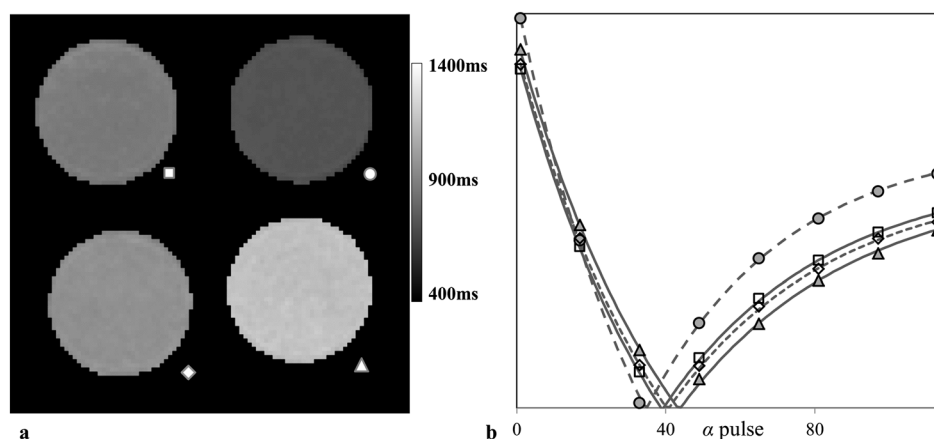


**Figure 6.** (a) The  $T_1$  map of the Ni-doped water phantoms using the elliptical Look-Locker (LL) acquisition with the goodness-of-fit (GOF) filter ( $\tau = 12.5$  ms;  $N_{\text{time}} = 8$ ;  $N_{\text{TL}} = 16$ ). The  $T_1$  maps show rather homogeneous  $T_1$  within all four tubes. (b) The LL data and fitted curves obtained from the center voxel in each tube. The four  $T_1$  values obtained from the curve fits are 817 ms (circle), 962 ms (square), 1056 ms (rhombus) and 1259 ms (triangle).

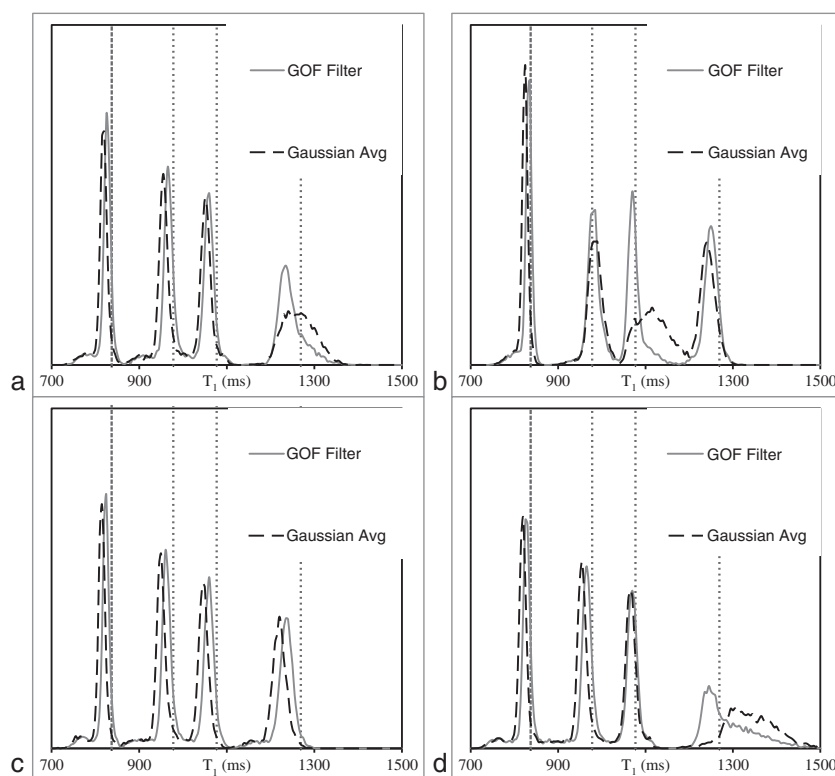


**Figure 7.** The  $T_1$  histograms of the Ni-doped water phantoms using different methods and parameters. Data acquired with: (a)  $\tau = 10$  ms;  $N_{\text{time}} = 10$ ;  $N_{\text{TL}} = 16$ ; (b)  $\tau = 15$  ms;  $N_{\text{time}} = 10$ ;  $N_{\text{TL}} = 8$ ; (c)  $\tau = 12.5$  ms;  $N_{\text{time}} = 8$ ;  $N_{\text{TL}} = 16$ ; (d)  $\tau = 16.7$  ms;  $N_{\text{time}} = 6$ ;  $N_{\text{TL}} = 16$ . The vertical lines are the  $T_1$  values acquired using the inversion recovery spin echo (IRSE) acquisition and are considered to be the true  $T_1$  values. In most cases, the distributions using the two-angle smoothing techniques produced  $T_1$  with very similar width. The goodness-of-fit (GOF)-filtered  $\alpha$  map generally produced  $T_1$  values that were closer to the true values. In three cases [third peak in (b) and fourth peak in (a) and (d)], the  $T_1$  distribution is non-Gaussian and is probably the result of incorrect  $\alpha$  estimation. The GOF filter is able to remove some of these possible false angle estimations.

and fourth peak in Fig. 7a, d), the  $T_1$  distribution was observed to be non-Gaussian. In almost all of these cases, the GOF filter was able to eliminate this non-Gaussian behavior.

Figure 8 shows the  $T_1$  maps of the phantoms that have a non-Gaussian distribution. From these examples, it appears that the

non-Gaussian part of the distribution is mainly the result of  $T_1$  overestimation at the water-glass boundary. The hyperintense ring is probably an artifact as the phantoms were homogeneous and the ring was not present in the  $T_1$  maps obtained from other parameters. Although the Gaussian-weighted averaging method

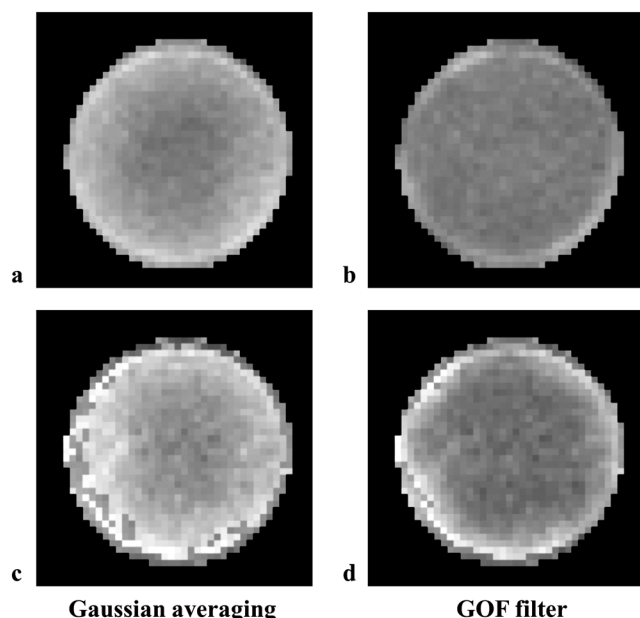


**Figure 8.**  $T_1$  maps of the Ni-doped phantoms. (a) and (b) correspond to the third peak in Fig. 7b; (c) and (d) correspond to the fourth peak in Fig. 7d. The window and level of the images are set to  $\pm 15\%$  of the actual  $T_1$  value. In these images, the hyperintense ring surrounding the water-glass interface is probably the result of incorrect angle estimation. The Gaussian-weighted averaged  $\alpha$  map appears to smear the hyperintense ring through the images as shown in (a) and (c). The goodness-of-fit (GOF)-filtered  $\alpha$  map, however, removes much of the rings as seen in (b) and (d).

smear the overestimated  $T_1$  as a diffuse hyperintense ring in Fig. 8a, c, the GOF-filtered  $\alpha$  map removed much of the hyperintensity in Fig. 8b. The GOF filter also appears to be more immune to incorrect angle estimation (Fig. 8d).

### In vivo animal study

Figure 9a–c shows the brain  $T_1$  maps acquired using the linear and elliptically segmented LL sequences and the corresponding slice acquired using the IRSE sequence. In general, the  $T_1$  maps based on the GOF filter were less noisy than those with the Gaussian-weighted averaged  $\alpha$  map. Otherwise, there were no other obvious differences in the  $T_1$  maps acquired with the LL acquisitions. Figure 9d, e shows the  $T_1$  distributions of the cortical gray matter (GM) and corpus callosum (CC) white matter (WM). We assumed that the  $T_1$  values obtained using the IRSE acquisition were the actual  $T_1$  values. The  $T_1$  distributions with elliptical segmentation and GOF filter were sharper and closer to the actual  $T_1$  distributions than were those of the linear segmentation. Table 3 summarizes the average  $T_1$  values in the cortical region and CC of the rat brain. Similar to the simulation and phantom studies described above, the average  $T_1$  values obtained with LL acquisitions were lower than the actual values. The average  $T_1$  values based on IRSE were within one standard deviation calculated from the LL acquisitions, with the exception of the  $T_1$  values in the CC region using linear segmentation. The GOF-filtered  $\alpha$  map generally reduced the standard deviation compared with the Gaussian-weighted averaged  $\alpha$  map. However, the elliptical segmentation produced  $T_1$  values closer to the actual values compared with the linear segmentation.

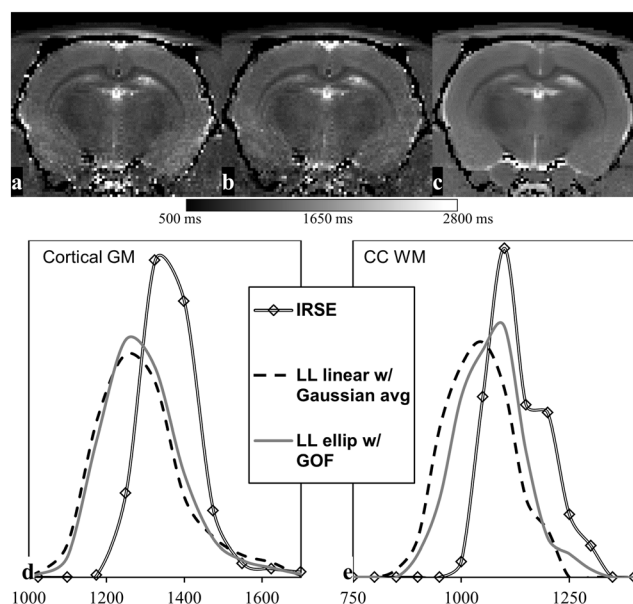


**Figure 9.**  $T_1$  maps of rat brain using: (a) Look-Locker (LL) acquisition with linear segmentation and Gaussian-weighted averaged  $\alpha$  map; (b) LL acquisition with elliptical segmentation and goodness-of-fit (GOF)-filtered  $\alpha$  map; (c) inversion recovery spin echo (IRSE) acquisition from the corresponding slice. A small surface coil superior to the brain was used in acquisition. As a result, lower signal-to-noise ratio (SNR) was observed at the bottom part of the image. In general, (a) and (b) appeared very similar, with image (a) appearing more noisy. IRSE has higher SNR because of the long TR, but its total scan time was too long to be of practical use. (d) and (e) show the  $T_1$  histograms of the cortical gray matter (GM) and corpus callosum (CC) white matter (WM). LL acquisition with elliptical segmentation and GOF filter produced distributions that were sharper and closer to IRSE values when compared with the traditional LL methods. Numerical comparisons are summarized in Table 3.

Table 4 shows the RMS differences between the LL and IRSE  $T_1$  maps. In the regions with high SNR, such as the cortex and CC, the RMS differences were below 200 ms. However, as a result of the physical limitation of the surface coil, parts of the entire  $T_1$  maps included regions with lower SNR. The overall RMS difference, including these low-SNR regions, increased to about 350 ms. In general, the combination of the elliptical segmentation and GOF filter reduced the RMS differences by about 1–5%, even when the comparison included the low-SNR regions. The one noticeable exception was the RMS difference in the CC, which was reduced by about 20% using the elliptical segmentation compared with the linear segmentation.

## DISCUSSION

In this study, we presented a modification to the LL acquisition scheme and introduced GOF filtering of the flip angle map to improve the quality of 3D  $T_1$  mapping using the LL sequence. We performed computer simulations, phantom studies and an *in vivo* animal brain study to evaluate the performance of these modifications.

The limitation of the 3D LL technique arises from the acquisition of each image at different magnetization states. This introduces intensity artifacts into the images and a negative bias in the  $T_1$

**Table 3.**  $T_1$  values (ms) of the cortical gray matter (GM) and white matter (WM) at the corpus callosum of the rat brain obtained from the  $T_1$  map shown in Fig. 9

	IRSE	LL linear with spatial averaging	LL linear with GOF filter	LL elliptical with spatial averaging	LL elliptical with GOF filter
GM	1416±126	1344±164	1332±136	1358±158	1342±130
WM	1157±66	1066±75	1068±74	1091±75	1090±75

GOF, goodness of fit; IRSE, inversion recovery spin echo; LL, Look-Locker.

**Table 4.** Root-mean-square (RMS) differences in the  $T_1$  values (ms) between the Look-Locker (LL) and inversion recovery spin echo (IRSE) acquisition schemes using the  $T_1$  maps shown in Fig. 9. The differences in the overall  $T_1$  values were calculated for the cortical gray matter (GM) and white matter (WM) at the corpus callosum

	LL linear with spatial averaging	LL linear with GOF filter	LL elliptical with spatial averaging	LL elliptical with GOF filter
GM	178	171	174	164
WM	104	102	83	84
Overall	370	361	337	333

GOF, goodness of fit.

estimation. We demonstrated, on the basis of the simulations, phantom and *in vivo* studies, that the elliptical LL segmentation can reduce the errors in  $T_1$  measurements compared with the linear segmentation. Application of the GOF filter to smooth the flip angle map can further reduce errors in the  $T_1$  estimation. The combination of both elliptical segmentation and the GOF filter was shown to improve the accuracy of  $T_1$  estimation. Larger improvements were seen at lower noise levels. At higher noise levels, however, the proposed methods yielded smaller improvement because the noise overshadows the artifacts. It is also worth noting that the elliptical segmentation appeared to greatly reduce errors in smaller regions, such as the CC in rat brain, as shown in our *in vivo* study.

It is worth noting that linear segmentation generally produces excessive errors along the  $k_y$  direction and relatively modest errors along the  $k_z$  direction. Compared with linear segmentation, elliptical segmentation reduces errors along the  $k_y$  direction; however, the errors along the  $k_z$  direction increase slightly. In the case in which  $T_1$  does not change along one direction, linear segmentation might perform better by setting  $k_y$  parallel to this direction. In all other cases, elliptical segmentation has the advantage because it reduces the overall error and artifacts as shown in our study.

We observed that the choice of parameters used in the LL acquisition can introduce artifacts that can be seen on the  $T_1$  maps. The presence of these artifacts appears to depend on the combination of  $T_1$  values and acquisition parameters. For example, in Fig. 3, the ripple artifact only occurred in one part of the image. Similarly, the ring artifact in the phantom studies only appeared in several tubes with selected LL acquisition parameters. One possible reason for the ring artifact could be the result of higher susceptibility at the interface of the glass wall and water. This artifact could not be eliminated by simple averaging alone. Conversely, the GOF filter significantly reduced/removed the artifacts by

eliminating the incorrect angles in the preliminary  $\alpha$  map. In addition to reducing the ring artifact, the GOF filter was also shown to decrease the negative bias in the  $T_1$  estimation in the phantom studies.

In this study, we assumed that the inversion angle  $\gamma$  did not deviate from the prescribed angle. The use of an adiabatic pulse for the inversion pulse perhaps justifies this assumption. As demonstrated by Kingsley *et al.* (23), the adiabatic pulse could deliver spin inversion with at least 99% efficiency, which corresponds to  $\gamma$  above  $172^\circ$ , in almost all cases. As suggested by Clare *et al.* (20), we also attempted to include  $\gamma$  in the curve fitting in our  $T_1$  calculation using the IRSE acquisition (results not shown). The fitted  $\gamma$  was  $175.5^\circ$  on average, and the resulting phantom  $T_1$  values increased between 0.2% and 0.4%. As the LL sequence utilized the same adiabatic pulse, similar variation in  $\gamma$  could be expected. In theory, fitting for  $\gamma$  can also be included in the analysis of LL data. Unfortunately, we found that, in most cases, there were a large number of combinations of  $T_1$ ,  $\alpha$  and  $\gamma$  that would yield the same  $\chi^2$  fitting if all three parameters were allowed to vary. The acquisition of more time points might ameliorate this problem. However, it would take a longer scan time, which may not be appropriate for *in vivo* studies, and, even then, the resolution of this problem is not guaranteed. As the difference is expected to be less than 0.5%, we fixed  $\gamma$  at  $180^\circ$ .

Several factors could affect the  $T_1$  mapping using the LL acquisition scheme. Published literature has shown that the choice of TI can affect the accuracy of  $T_1$  estimation using an IRSE sequence (24). Similarly, different selections of  $\tau$  and  $N_{\text{time}}$  in an LL acquisition have been shown to have an impact on the results of  $T_1$  computation (see Fig. 7). With all the parameter combinations tested, the results obtained from different parameters were all within 3% of each other when using the GOF filter.



The use of Equation [1] relies on two conditions: the transverse magnetization is completely spoiled before each RF pulse and the magnetization is in steady state. In this study, we used both the RF and gradient spoiling methods. A standard RF spoiler with  $117^\circ$  increment from  $\alpha$  pulse to  $\alpha$  pulse was applied (25). The strength of the gradient spoiler was determined by increasing the gradient amplitude and/or duration in the SPGR sequence until the signal reached an asymptotic value. Based on our study, it appears that a gradient amplitude of 150 mT/m applied for 4 ms is sufficient. The two spoiling methods should create sufficient incoherence in the transverse magnetization. In addition, an adequate number of dummy scans is necessary to drive the magnetization into steady state. Using a Bloch simulator (26), we found that  $N_{\text{dummy}} = 5$  is needed to reach steady state if  $T_1$  is below 1800 ms. If  $T_1$  is 3000 ms, a value of  $N_{\text{dummy}} = 7$  is required.

In conclusion, the proposed elliptical segmentation scheme, in combination with GOF  $\alpha$  map filtering, has been shown to improve the accuracy and reduce the artifacts in the  $T_1$  map using 3D LL acquisition.

## Acknowledgements

We thank Dr Juan Herrera for preparing the animal and Dr Richard Wendt for providing the SpinWright Bloch simulator. This study was supported in part by the Department of Defense (grant number PT074693P10) and the National Institutes of Health (NIH) (grant number R01 EB02095). Funding for the 7-T MRI scanner was provided by NIH grant number S10 RR17205.

## REFERENCES

- Christensen KA, Grant DM, Schulman EM, Walling C. Optimal determination of relaxation times of Fourier transform nuclear magnetic resonance. Determination of spin-lattice relaxation times in chemically polarized species. *J. Phys. Chem.* 1974; 78(19): 1971–1977.
- Kaldoudi E, Williams SCR. Relaxation time measurements in NMR imaging. Part I: Longitudinal relaxation time. *Concepts Magn. Reson.* 1993; 5(3): 217–242.
- Parker GJM, Barker GJ, Tofts PS. Accurate multislice gradient echo T1 measurement in the presence of non-ideal RF pulse shape and RF field nonuniformity. *Magn. Reson. Med.* 2001; 45(5): 838–845.
- Venkatesan R, Lin W, Haacke EM. Accurate determination of spin-density and T1 in the presence of RF-field inhomogeneities and flip-angle miscalibration. *Magn. Reson. Med.* 1998; 40(4): 592–602.
- Cheng HL, Wright GA. Rapid high-resolution T1 mapping by variable flip angles: accurate and precise measurements in the presence of radiofrequency field inhomogeneity. *Magn. Reson. Med.* 2006; 55(3): 566–574.
- Deoni SCL, Rutt BK, Peters TM. Rapid combined T1 and T2 mapping using gradient recalled acquisition in the steady state. *Magn. Reson. Med.* 2003; 49(3): 515–526.
- Preibisch C, Deichmann R. Influence of RF spoiling on the stability and accuracy of T1 mapping based on spoiled FLASH with varying flip angles. *Magn. Reson. Med.* 2009; 61(1): 125–135.
- Look DC, Locker DR. Time saving in measurement of NMR and EPR relaxation times. *Rev. Sci. Instrum.* 1970; 41(2): 250–251.
- Deichmann R, Haase A. Quantification of T1 values by SNAPSHOT-FLASH NMR imaging. *J. Magn. Reson.* 1992; 96(3): 608–612.
- Deichmann R, Hahn D, Haase A. Fast T1 mapping on a whole-body scanner. *Magn. Reson. Med.* 1999; 42(1): 206–209.
- Shah NJ, Zaitsev M, Steinhoff S, Zilles K. A new method for fast multislice T1 mapping. *Neuroimage*, 2001; 14(5): 1175–1185.
- Steinhoff S, Zaitsev M, Zilles K, Shah NJ. Fast T1 mapping with volume coverage. *Magn. Reson. Med.* 2001; 46(1): 131–140.
- Henderson E, McKinnon G, Lee T-Y, Rutt BK. A fast 3D Look-Locker method for volumetric T1 mapping. *Magn. Reson. Imaging*, 1999; 17(8): 1163–1171.

- Gai ND, Butman JA. Modulated repetition time Look-Locker (MORTLL): a method for rapid high resolution three-dimensional T1 mapping. *J. Magn. Reson. Imaging*, 2009; 30(3): 640–648.
- Nkongchu K, Santyr G. An improved 3-D Look-Locker imaging method for T1 parameter estimation. *Magn. Reson. Imaging*, 2005; 23(7): 801–807.
- Wartjes JBM, Dahlqvist O, Lundberg P. Novel method for rapid, simultaneous T1, T2\*, and proton density quantification. *Magn. Reson. Med.* 2007; 57(3): 528–537.
- Blüml S, Schad LR, Stepanow B, Lorenz WJ. Spin-lattice relaxation time measurement by means of a TurboFLASH technique. *Magn. Reson. Med.* 1993; 30(3): 289–295.
- Wilman AH, Riederer SJ. Performance of an elliptical centric view order for signal enhancement and motion artifact suppression in breath-hold three-dimensional gradient echo imaging. *Magn. Reson. Med.* 1997; 38(5): 793–802.
- Deichmann R. Fast high-resolution T1 mapping of the human brain. *Magn. Reson. Med.* 2005; 54(1): 20–27.
- Clare S, Jezzard P. Rapid T1 mapping using multislice echo planar imaging. *Magn. Reson. Med.* 2001; 45(4): 630–634.
- Markwardt CB. Non-linear least-squares fitting in IDL with MPFIT. *Proceedings of Astronomical Data Analysis Software and Systems XVIII*, Quebec City, QC, Canada, 2009; 251–254.
- Nehrke K. On the steady-state properties of actual flip angle imaging (AFI). *Magn. Reson. Med.* 2009; 61(1): 84–92.
- Kingsley PB, Ogg RJ, Reddick WE, Steen RG. Correction of errors caused by imperfect inversion pulses in MR imaging measurement of T1 relaxation times. *Magn. Reson. Imaging*, 1998; 16(9): 1049–1055.
- Ogg RJ, Kingsley PB. Optimized precision of inversion-recovery T1 measurements for constrained scan time. *Magn. Reson. Med.* 2004; 51(3): 625–630.
- Zur Y, Wood ML, Neuringer LJ. Spoiling of transverse magnetization in steady-state sequences. *Magn. Reson. Med.* 1991; 21(2): 251–263.
- Wendt RE. SpinWright: a simulation of the Bloch equations for teaching magnetic resonance principles. *Med. Phys.* 2002; 29(6): 1312.

## APPENDIX A. DERIVATION OF THE TRANSVERSE MAGNETIZATION IN AN LL ACQUISITION

The LL sequence is composed of an inversion pulse  $\gamma$  followed by a series of small flip angle pulses  $\alpha$  to acquire SPGR images. Let  $M_n^-$  and  $M_n^+$  be the longitudinal magnetization immediately before and after the  $n^{\text{th}}$   $\alpha$  pulse following the inversion. Then:

$$M_n^+(0) = M_n^- \cos \alpha \quad [\text{A1}]$$

The  $(n+1)^{\text{th}}$  pulse is applied at time  $\tau$  after the  $n^{\text{th}}$  pulse, so:

$$M_n^+(\tau) = M_0 \left( 1 - e^{-\tau/T_1} \right) + M_n^- \cos \alpha e^{-\tau/T_1} = M_{n+1}^- \quad [\text{A2}]$$

Let  $N_{\text{tot}}$  be the total number of  $\alpha$  pulses applied after each inversion, and  $M_\gamma^-$  be the longitudinal magnetization immediately before the  $\gamma$  pulse. The  $\gamma$  pulse is applied at time  $t_r$  after the last  $\alpha$  pulse ( $N_{\text{tot}}$ ). Therefore, the magnetization immediately prior to the application of the  $\gamma$  pulse is given by:

$$M_\gamma^- = M_{N_{\text{tot}}}^+ (t_r) = M_0 \left( 1 - e^{-t_r/T_1} \right) + M_{N_{\text{tot}}}^- \cos \alpha e^{-t_r/T_1} \quad [\text{A3}]$$

The magnetization after the  $\gamma$  pulse is:

$$M_\gamma^+(0) = M_\gamma^- \cos \gamma = \left[ M_0 \left( 1 - e^{-t_r/T_1} \right) + M_{N_{\text{tot}}}^- \cos \alpha e^{-t_r/T_1} \right] \cos \gamma \quad [\text{A4}]$$

It should be noted that Equation [A4] also holds for the saturation recovery sequence, where  $\gamma$  is  $90^\circ$  instead of  $180^\circ$ . The first  $\alpha$  pulse is applied at time  $t_d$  after the  $\gamma$  pulse; therefore, the longitudinal magnetization immediately before the first  $\alpha$  pulse is:

$$M_1^- = M_0(1 - e^{-t_d/T_1}) + M_\gamma^- \cos \gamma e^{-t_d/T_1} \quad [A5]$$

The following simplified notation is used:

$$\begin{aligned} E\tau &= \exp(-\tau/T_1) \\ Ed &= \exp(-t_d/T_1) \\ Er &= \exp(-t_r/T_1) \end{aligned}$$

Therefore, the magnetization immediately before the  $n^{\text{th}}$   $\alpha$  pulse is:

$$\begin{aligned} M_n^- &= M_0(1 - E\tau) \left[ 1 + \cos \alpha E\tau + (\cos \alpha E\tau)^2 + \dots + (\cos \alpha E\tau)^{n-2} \right] \\ &+ [M_0(1 - Ed) + M_\gamma^- \cos \gamma Ed] (\cos \alpha E\tau)^{n-1} \end{aligned} \quad (A6)$$

The series in the first term can be summed and Equation [A6] yields:

$$\begin{aligned} M_n^- &= M_0 \left\{ \frac{1 - E\tau}{1 - \cos \alpha E\tau} (1 - (\cos \alpha E\tau)^{n-1}) + \frac{(\cos \alpha E\tau)^{n-1}}{1 - \cos \gamma Ed \cos \alpha Er (\cos \alpha E\tau)^{N_{\text{tot}}-1}} \right. \\ &\times \left. \left[ 1 - (1 - \cos \gamma)Ed - \cos \gamma Ed Er + (1 - E\tau) \cos \gamma Ed \cos \alpha Er \left( \frac{1 - (\cos \alpha E\tau)^{N_{\text{tot}}-1}}{1 - \cos \alpha E\tau} \right) \right] \right\} \end{aligned} \quad (A9)$$

$$\begin{aligned} M_n^- &= M_0(1 - E\tau) \left[ \frac{1 - (\cos \alpha E\tau)^{n-1}}{1 - \cos \alpha E\tau} \right] \\ &+ [M_0(1 - Ed) + M_\gamma^- \cos \gamma Ed] (\cos \alpha E\tau)^{n-1} \end{aligned} \quad (A7)$$

Combining Equation [A3] with Equation [A6],  $M_\gamma^-$  under steady-state conditions can be calculated:

$$\begin{aligned} M_\gamma^- &= M_0(1 - Er) + \left\{ M_0(1 - E\tau) \left[ \frac{1 - (\cos \alpha E\tau)^{N_{\text{tot}}-1}}{1 - \cos \alpha E\tau} \right] \right. \\ &+ [M_0(1 - Ed) + M_\gamma^- \cos \gamma Ed] (\cos \alpha E\tau)^{N_{\text{tot}}-1} \left. \right\} \cos \alpha Er \\ &\Rightarrow (1 - \cos \gamma Ed \cos \alpha Er (\cos \alpha E\tau)^{N_{\text{tot}}-1}) M_\gamma^- \\ &= M_0 \left\{ (1 - Er) + (1 - E\tau) \left[ \frac{1 - (\cos \alpha E\tau)^{N_{\text{tot}}-1}}{1 - \cos \alpha E\tau} \right] \right. \\ &+ (1 - Ed) (\cos \alpha E\tau)^{N_{\text{tot}}-1} \cos \alpha Er \left. \right\} \end{aligned}$$

which leads to

$$\begin{aligned} M_\gamma^- &= \frac{M_0}{1 - \cos \gamma Ed \cos \alpha Er (\cos \alpha E\tau)^{N_{\text{tot}}-1}} \\ &\times \left\{ (1 - Er) + (1 - E\tau) \left[ \frac{1 - (\cos \alpha E\tau)^{N_{\text{tot}}-1}}{1 - \cos \alpha E\tau} \right] \right. \\ &+ (1 - Ed) (\cos \alpha E\tau)^{N_{\text{tot}}-1} \cos \alpha Er \left. \right\} \end{aligned} \quad (A8)$$

Substituting  $M_\gamma^-$  in Equation (A8) into Equation [A7] yields:

The transverse magnetization  $M_\perp(n)$  is equal to  $M_n^- \sin \alpha$ , which is represented in Equation [1].